Innovative TEM-coupled approaches to study foraminiferal cells

Hidetaka Nomaki[a], Charlotte LeKieffre[b], Stéphane Escrig[b], Anders Meibom[b,c], Shinsuke Yagyu[d], Elizabeth A. Richardson[e], Takuya Matsuzaki[d], Masafumi Murayama[d], Emmanuelle Geslin[f], Joan M. Bernhard[g]

[a] Department of Biogeochemistry, Japan Agency for Marine-Earth Science and Technology, 2-15 Natsushima-cho, Yokosuka, Kanagawa, 237-0061, Japan

[b] Laboratory for Biological Geochemistry, School of Architecture, Civil and Environmental Engineering (ENAC), Ecole Polytechnique Fédérale de Lausanne (EPFL), 1015 Lausanne, Switzerland

[c] Center for Advanced Surface Analysis, Institute of Earth Sciences, University of Lausanne, Switzerland

[d] Center for Advanced Marine Core Research, Kochi University, B200, Monobe, Nankoku-city, Kochi, 783-8502, Japan

[e] Georgia Electron Microscopy, University of Georgia, Athens, GA 30602, USA

[f] LPG-BIAF, University of Angers, UMR CNRS 6112, 49095 Angers Cedex, France

[g] Department of Geology and Geophysics, Woods Hole Oceanographic Institution, Woods Hole, MA 02543, USA

* Corresponding author: nomakih@jamstec.go.jp

Key words: Ultrastructure, NanoSIMS, micro-X-ray CT, correlative microscopy, isotope mapping, microhabitat

Abstract

Transmission electron microscope (TEM) observation has revealed much about the basic cell biology of foraminifera. Yet, there remains much we do not know about foraminiferal cytology and physiology, especially for smaller benthic foraminifera, which inhabit a wide range of habitats. Recently, some TEM-coupled approaches have been developed to study correlative foraminiferal ecology and physiology in detail: Fluorescently Labeled Embedded Core (FLEC)-TEM for observing foraminiferal life-position together with their cytoplasmic ultrastructure, micro-X-ray computed tomography (CT)-TEM for observing and reconstructing foraminiferal cytoplasm in three dimensions (3D), and TEM-Nanometer-scale secondary ion mass spectrometry (NanoSIMS) for mapping of elemental and isotopic compositions at sub-micrometer resolutions with known ultrastructure. In this contribution, we review and illustrate these recent advances of TEM-coupled methods.

1. Introduction

Benthic foraminifera are unicellular eukaryotes that are abundant constituents of the marine seafloor. Their habitats are diverse and, thus, as a group they encounter many different environmental conditions such as temperature, salinity, dissolved oxygen concentrations, water depths, trophic conditions, and redox conditions (reviewed in Murray 2006). It is expected that foraminifera have physiological adaptations to these various environments. Studies of their cytoplasmic structure are therefore keys to understanding how these microbial eukaryotes adapt to those different environmental conditions. Ultrastructural observation using a transmission electron microscope (TEM) has successfully been applied to foraminifera since the 1960s (Hedley et al. 1967; Dahlgren 1967a, b). The relationships between foraminiferal cellular ultrastructure and environments have been studied in a few cases (e.g., Leutenegger and Hansen 1979; Bernhard and Bowser 2008; Bernhard et al. 2006a, 2010a; 2010b). For instance, *Virgulinella fragilis,* which can thrive in micro-oxic and hydrogen sulfide-enriched environments, is known to support a double symbiosis with kleptoplasts and putative δ-proteobacteria (Bernhard 2003; Tsuchiya et al. 2015). Although ultrastructural observations have cast light on many different aspects of foraminiferal metabolic diversity, TEM observation alone is not enough to determine the functions of all organelles. For example, incubation experiments are needed to establish the function of putative "symbionts" such as photosynthetic kleptoplasts (e.g., Jauffrais et al. 2016, 2017).

Also, recent advances on fine-scale analyses of porewater chemistry in sediments indicate both vertical and horizontal gradients and heterogeneity of constituents such as oxygen (Glud et al. 2005), nitrate (Glud et al. 2009; Metzger et al., 2016), dissolved reactive phosphorus, dissolved iron (Thibault de Chanvalon et al. 2015), and probably other compounds as well, at sub-millimeter length scales. Many benthic foraminifera are infaunal, particularly in mesotrophic to eutrophic sediments where they can utilize organic matter even in deep sediments (e.g., >3 cm below the sediment-water interface; Jorissen et al. 1995). The micro-environments of infaunal foraminifera are, thus, highly diverse and heterogeneous, and can change temporally (Glud et al. 2005). Although foraminifera are able to migrate within sediments (Alve and Bernhard 1995; Moodley et al. 1998; Gross 2000; Heinz et al. 2001; Geslin et al., 2004; Nomaki et al. 2005; Koho et al. 2011), the ultrastructural characteristics observed with the TEM are likely to reflect the micro-environments that cannot be characterized with bulk-sediment analysis.

Recently, innovative methods using the TEM and coupled recent microanalytical technologies have been developed and applied to foraminiferal studies in efforts to overcome these challenges. The Fluorescently Labeled Embedded Core (FLEC) method is an excellent approach to reveal foraminiferal life position in sediments. The fluorescent tags are used to label metabolically active cells in sediments and their positions are maintained in the

sediments with glutaraldehyde fixation and subsequent resin embedding. Because FLEC also labels additional organisms like ciliates and prokaryotes, it is also possible to observe interactions between foraminifera and these organisms together with foraminiferal ultrastructure observed with the TEM of the same sliced plane.

The complete sequential thin-section analysis of a whole organism or an array-tomography technique can be applied to study small-sized specimens (Yabuki et al. 2012, 2013; Micheva and Smith 2007). Because foraminifera are relatively large cells (hundreds of μm), however, the complete ultrastructure of an entire foraminifera is difficult to reconstruct from TEM observations. One solution to the foraminiferal size issue is micro-X-ray computed tomography (CT), which also provides information on internal structures. Micro-X-ray CT has been used to assess attributes regarding foraminiferal tests (shells), such as biometry (Speijer et al. 2008; Briguglio et al. 2011, 2013; Hohenegger and Briguglio 2012; Ferrández Cañadell et al. 2014) and test-wall dissolution by means of X-ray attenuation (Johnstone et al. 2010; Iwasaki et al. 2015). Nomaki et al. (2015) applied X-ray CT to foraminiferal cells prepared for TEM (i.e., resin embedded; stained with heavy metals). Because micro-X-ray CT is nondestructive, observations of foraminiferal cytoplasmic structure with this technique prior to sectioning for TEM allow us to determine the precise positioning of sections that have particular cytoplasmic structures, such as extended reticulopodia, the cell periphery, chamber plugs, vacuoles, or multiple nuclei. The X-ray CT can also determine the surface area and volume of foraminiferal cytoplasm and selected structures, thus, permitting quantitative analyses of foraminiferal biovolume and growth pattern through chamber addition, as well as allowing an estimation of volumes and surface areas of vacuoles, which contain soluble compounds (Khalifa et al. 2016).

The combination of TEM and Nanometer-scale secondary ion mass spectrometry (NanoSIMS) can spatially investigate the elemental and isotopic compositions of organisms at sub-micrometer resolution (e.g., Finzi-Hart *et al*. 2009; Pernice et al. 2012; Carpenter *et al*. 2013; Hoppe et al., 2013; Kopp *et al*. 2015). In pulse-chase experiments with isotopically labeled substrates, it is therefore possible to quantitatively evaluate where within a cell, such as specific organelle types or endobionts, a certain molecule or its metabolic derivates were located at a given point in time (Nomaki et al. 2016; LeKieffre et al. 2017).

Here, we present three advanced TEM-coupled technologies applied to foraminiferal research; FLEC-TEM; micro-X-ray CT-TEM, and TEM-NanoSIMS. All these TEM-related methods provide valuable information on foraminiferal biology and ecology. Examples of these correlative technologies are presented along with summaries of each method, notes regarding advantages and disadvantages, and possible future applications.

2. Materials and Procedures

2.1. FLEC-TEM

Specimens were prepared using the FLEC-TEM method described by Bernhard and Richardson (2014). Foraminifera-bearing sediment cores were collected between July 23-25, 2007 from an area off Monterey, California (USA) with active hydrocarbon seepage, at approximately 36°44.7'N 122°16.6'W (~1003 m water depth; Bernhard et al. 2010b), using pushcorers manipulated by the ROV *Jason*. The viability indicator CellTracker Green CMFDA (Thermo Fisher Scientific; Bernhard *et al.*, 2006b) was injected into the pushcores and allowed to incubate *in situ* for approximately 1 day (Bernhard et al. 2009). For this study, two pushcores were utilized. One core, designated as the seep core, was collected adjacent to a clam bed (Bernhard et al., 2010b) while the other, designated the non-seep core, was collected >25 m from visible active seepage. Aboard the surface vessel RV *Atlantis*, each core was subsampled with 1.5-cm diameter syringe cores, which were preserved in ~3% glutaraldehyde / 0.1 M cacodyllic acid (pH 7.2). At WHOI (USA), syringe cores were further processed for FLEC as described in Bernhard and Bowser (1996) and Bernhard et al. (2003). Polymerized FLEC cores were sectioned perpendicular to the sediment-water interface using a Beuhler Low Speed Saw for rocks. Resulting sections were ~0.5mm in thickness. Fluorescent foraminifera were observed using an epifluorescence-equipped dissecting microscope (Leica FLIII with fluorescein / Green Fluorescent Protein filters; 490-nm bandpass excitation; 520-nm bandpass emission), which was used to note foraminiferal location in sediment slices along with their depth below the sediment-water interface. Select foraminifera were further imaged with an Olympus Fluoview Laser Scanning Confocal Microscope (LSCM) and then excised from their FLEC sediment slice using a sharp razor blade. Foraminifera were identified using morphology, test texture (mineralized vs. agglutinated), and knowledge of the local foraminiferal assemblage. In many cases, identification to species was not possible.

Blocks were trimmed as appropriate for TEM (Bernhard and Richardson, 2014), and sectioned with Diatome diamond knives into 1-µm thick sections for light microscopy and 70-nm thin sections for transmission electron microscopy. Thick sections were stained with toluidine blue and imaged with a Zeiss Axiovert 40C Tissue Culture microscope. Thin sections were post-stained with a solution of uranyl acetate (4%) in ethanol and a modified version of Sato's lead citrate (Hanaichi et al., 1986). Transmission electron microscopy observations were made using a Zeiss 10CA TEM at the Marine Biological Laboratory (Woods Hole, MA, USA) or a JEOL JEM1011 TEM at the Georgia Electron Microscopy facility, University of Georgia (Athens, GA, USA).

2.2. Micro-X-ray CT

2.2.1. Foraminiferal sampling and fixation

154 The intertidal foraminifera *Ammonia* sp. (phylotype T6; Holzmann 2000, Hayward et
155 al. 2004) was collected from the Nojima tidal flat (35°19.4N 139°38.1E; water depth, ~0 m)
156 of Tokyo Bay on March 21, 2014. The deep-sea foraminiferal samples were collected from
157 central Sagami Bay, Japan (35°01.3N 139°22.1E; water depth 1430 m), during a cruise of
158 *R/V Kaimei* KM16-01 in April 2016. At the Nojima tidal flat, the top ~1 cm of sediment was
159 collected into several 4 L buckets for foraminiferal fixation in the laboratory. For Sagami Bay,
160 sediment samples collected with a push corer were immediately sliced onboard into 0.5- or
161 1-cm sections to a depth of 6 cm. The sediment samples were fixed in 10% glutaraldehyde in
162 cacodylate buffer to a final concentration of 4.0% glutaraldehyde. In the laboratory,
163 specimens that had an aggregation of sediment particles around their aperture and/or whose
164 test was mostly filled with cytoplasm were isolated from the >125-*μ*m size fraction using a
165 binocular stereomicroscope.
166
167 2.2.2. Post-fixation, staining and embedding into resin
168 Sample post-fixation using osmium tetroxide, staining with uranyl acetate, and
169 subsequent embedding into resin block followed the protocol for micro-X-ray and TEM
170 sample preparation described previously (Nomaki et al. 2015). To yield high-contrast
171 specimens for X-ray CT analysis, specimens were post-fixed and stained with osmium
172 tetroxide and uranyl acetate. Osmium tetroxide is a conventional post-fixation agent that
173 preserves lipids, and also some amino acids, peptides, and proteins to a lesser extent (Hayat
174 2000). Uranyl acetate stains nucleic acids and, to a lesser extent, proteins (Hayat 2000).
175
176 2.2.3. Micro-X-ray CT imaging
177 The resin-embedded Os- and U-stained foraminiferal specimens were imaged using a
178 model Xradia 410 Versa microfocus X-ray CT system (Zeiss). An X-ray filter was attached to
179 the X-ray source to reduce the X-ray energy to yield better resolution. The X-ray source
180 setting was 40 kV and 200 μA for *Bolivina spissa*, and the exposure time for each projection
181 was 10 seconds. A total of 1601 projections were performed during 360° rotation and the
182 resolution of the obtained image was 1.07 μm/pixel. For *Ammonia* sp. (phylotype T6),
183 different settings were applied: 60 kV and 130-μA X-ray source with 5 second projection for
184 a total of 801 projections per 360° rotation. The short projection time and lower numbers of
185 projections for *Ammonia* sp. (phylotype T6) resulted in lower quality images compared to
186 those of *B. spissa*. The obtained data were reconstructed using the manufacturer-supplied
187 software and Osirix MD 6.5 (Pixmeo) software.
188
189
190 2.3. TEM-NanoSIMS
191 TEM-NanoSIMS analyses of benthic foraminifera was conducted independently in

two different laboratories. Although the principal methods for our two sets of correlative TEM-NanoSIMS analyses were similar, there are several minor differences between Nomaki et al. (2016) and LeKieffre et al. (in press), as summarized in Tables 1 and 2. Below we describe similarities and differences in methodology.

2.3.1. Incubation with stable-isotope tracer(s)

Benthic foraminifera collected from Nojima tidal flat (Japan), Bourgneuf Bay (France), or Gullmar Fjord (Sweden) (Table 1, Nomaki et al. 2016, LeKieffre et al. in press and unpublished data) were incubated for different durations with different isotope tracers (as noted below). *Ammonia* sp. (phylotype T6) collected from the Nojima tidal flat were incubated with sediment either in dysoxic or anoxic conditions. Foraminifera were isolated from Bourgneuf Bay sediments (*Ammonia* sp. phylotype T6 and *Haynesina germanica*) and Gullmar Fjord sediments (*Nonionellina labradorica*) and incubated without sediments in artificial seawater (ASW, RedSea salt, salinity: 35). All foraminiferal specimens were incubated with additions of ^{13}C, ^{15}N, or ^{34}S tracer(s) (Table 1, Nomaki et al. 2016; LeKieffre et al. in press and unpublished data).

2.3.2. Fixation and embedding into resin

After isotopic incubations, the Nojima flat sediments including benthic foraminifera were fixed in 10% glutaraldehyde in cacodylate buffer to a final concentration of 4.0% glutaraldehyde. Specimens whose tests (except for the ultimate one or two chambers) were filled with bright yellow cytoplasm typical of this *Ammonia* sp. (phylotype T6) were selected for analysis. Foraminifera from Bourgneuf Bay and Gullmar Fjord were, at the end of their incubation in isotope-spiked ASW, immediately fixed according to the chemical fixation protocol described in LeKieffre et al. (this issue). These glutaraldehyde-fixed foraminiferal specimens were either embedded in agarose (Nomaki et al. 2016) or directly decalcified (LeKieffre et al., in press), and then all specimens were post-fixed using osmium tetroxide. The Nojima specimens were additionally stained with uranyl-acetate “en-bloc” for 2 h followed by rinsing with distilled water. All samples were subsequently embedded in resin (Nomaki et al. 2016, LeKieffre et al. this issue, Koho et al. this issue).

2.3.3. Sectioning, TEM imaging and coating

Embedded specimens were sectioned into ultra-thin (60-nm to 70-nm thick) or semi-thin (200-nm thick) sections. Sections were transferred to copper grids and stained with 2% aqueous uranyl acetate only (LeKieffre et al. in press) or 2% aqueous uranyl acetate followed by 0.3% lead nitrate and 0.3% lead acetate solution (Nomaki et al. 2016). In Nomaki et al. (2016), specimens’ ultra-thin sections were used for detailed observations of organelle membranes to check cell integrity (e.g., intact mitochondrial cristae and

double-membranes); semi-thin sections were used for subsequent TEM-NanoSIMS analyses. In the case of LeKieffre et al. (in press) materials, the same ultra-thin sections were used for both TEM and NanoSIMS. Once the target area for NanoSIMS analyses was selected, that targeted region was observed sequentially and a composite of TEM images was reconstructed. TEM-imaged sections intended for NanoSIMS analysis were coated with 20 nm of osmium (Nomaki et al. 2016) or 10 nm of gold (LeKieffre et al. in press) to prevent samples from electron charging during NanoSIMS analysis.

2.3.4. NanoSIMS measurements

Grids containing metal-coated sections were placed into the sample holder of a nanometer-scale secondary ion mass spectrometer (NanoSIMS NS50 or NanoSIMS 50L). The settings of the NanoSIMS analyses are summarized in Table 2.

During analysis, secondary ions were extracted with a primary Cs^+ beam. Different settings were used for the Cs^+ beam, resulting in a slightly different primary beam spot size on the two instruments) (Table 2). A multi-collector system was used to simultaneously measure five to seven different secondary ions (Nomaki et al. 2016; LeKieffre et al. in press). Areas of 8 × 8-µm to 30 × 30-µm were imaged with either 128 × 128 or 256 × 256 pixels rastered images. Sequential layers of images (up to 50) were accumulated to produce one image for each given area. The data quantification was performed after a drift correction of all layers, using the software ImageJ or L'IMAGE developed by Dr. Larry Nittler, Carnegie Institution of Washington, USA.

2.3.5. Data analysis

Correlation between NanoSIMS and TEM images was done by aligning the $^{12}C^{14}N^-$ ion image with the corresponding ultrastructural features in a TEM image. Values of ^{15}N and ^{34}S enrichments were obtained from the $^{12}C^{15}N^-/(^{12}C^{14}N^- + {}^{12}C^{15}N^-)$ or $^{12}C^{15}N^-/{}^{12}C^{14}N^-$ and $^{34}S^-/(^{32}S^- + {}^{34}S^-)$ or $^{34}S^-/{}^{32}S^-$ ratios respectively, and presented as ‰ enrichment over the natural isotope ratio measured in unlabeled samples prepared and analyzed identically. These ratios were calculated for selected regions of interest, using the program Look@NanoSIMS (Polerecky et al., 2012). This allows comparison of different cell compartments within the cytoplasm, or between different time points or incubation conditions (e.g., pH, light, salinity, temperature, oxygen, presence/absence of a certain nutrient). It is noted that comparisons of isotopic ratios between samples from experiments using different sample preparation methods should be treated with caution as differences in sample preparation can lead to different isotopic ratios (Musat et al., 2014). For the data presented here, such effects did not significantly impact data interpretations.

3. Results and Discussions

268

269 3.1. FLEC-TEM

270 3.1.1. Results

271 Here, two foraminifera were designated for fluorescently labeled embedded core
272 (FLEC)-TEM analyses, one individual from each ROV-collected core. In the non-seep core,
273 the specimen was located at a sediment depth of 1.7 cm below the sediment-water interface.
274 The upper edge of the core section shown in Fig. 1A was not the sediment-water interface.
275 This specimen was tentatively identified as a *Buliminella tenuata* due to knowledge of the
276 area's foraminiferal community (Bernhard et al., 2001; Bernhard et al., 2010b); it appeared to
277 have intact cytoplasmic vacuoles in LSCM images (Fig. 1B). The test of this specimen was
278 calcite, as evidenced by its appearance in reflected light (Fig. 1A) and in semi-thin section
279 (Fig. 1C). The ultimate chamber of this individual contained little cytoplasm (Fig. 1B, C),
280 which is to be expected given this is where reticulopods are deployed and retracted through
281 the aperture (e.g., Alexander and Banner, 1984). This specimen also appeared to have a
282 distinct layer of fluorescent material attached to the test (shell) exterior, as noted in the
283 LSCM micrograph (Fig. 1B). In the sediments, the specimen was slightly inclined from
284 horizontal, with the apertural end oriented deepest (Fig. 1B, C). What appears to be an open
285 pore space is adjacent to the specimen's aperture (Fig. 1B, C).

286 In TEM micrographs of *B. tenuata* from the non-seep core, large vacuoles were
287 visible (Fig. 2A). It is notable that osmication is not included in the FLEC-TEM preparation
288 procedure. Thus, the membranes in FLEC-TEM specimens do not appear as distinctly as
289 those membranes observed in specimens that were conventionally prepared for TEM (i.e.,
290 with osmication). What appeared to be degradation vacuoles (i.e., food vacuoles; see
291 LeKieffre et al., this issue) were relatively common (Fig. 2A, B), containing items appearing
292 to be prokaryotes as well as unidentifiable materials. Mitochondria were identified by their
293 shape and size (Fig. 2B-D); in some cases cristae and the double membrane were discernable
294 (Fig. 2C), but not clearly. The mitochondria appeared to occur at the cell periphery, as well as
295 far from the periphery, well within the cell. Electron-opaque bodies, sensu LeKieffre et al.
296 (this issue) (also known as "electron dense bodies"; Nomaki et al., 2016), were also observed
297 (Fig. 2C-E). Golgi were also noted (Fig. 2 B-D), as were peroxisomes with endoplasmic
298 reticulum (Fig. 2E). The crystalized core (catalase) of peroxisomes (Fig. 2E inset; Bernhard
299 and Bowser, 2008) was not as distinctive in these preparations compared to those subject to
300 conventional TEM processing with osmication. There was no evidence of prokaryotic
301 endobionts (i.e., endosymbionts) in this foraminiferan. Examination of the area immediately
302 adjacent to what would have been the test exterior revealed that the fluorescent material
303 observed in the LSCM image (Fig. 1B) was not prokaryotic (i.e., ectobionts) but was most
304 likely foraminiferal reticulopods (Fig. 2F, G). Because we did not fix the FLEC cores to
305 preserve reticulopods (Travis and Bowser 1986, Bernhard et al., 2013), well-preserved

306 reticulopodial networks were not expected, but such structures (Fig. 2F, G) are not
307 inconsistent with reticulopodial cytoplasm.
308 The foraminifer from the seep core was agglutinated, evidenced by the brownish color
309 of the test (Fig. 3A), especially when compared to a calcareous (white) foraminifer in the
310 same image. This agglutinated seep specimen was clearly biserial but we were not confident
311 in identifying this specimen to a genus or species. The specimen aperture was located at a
312 sediment depth of 1.7 mm below the sediment-water interface (Fig. 3A, B), near a juvenile
313 clam. Microbes (eukaryotes and/or prokaryotes) also occurred in these sediments (Fig. 3B),
314 but no additional foraminifera visible in reflected light (Fig. 3A) were living (i.e., fluorescent;
315 Fig. 3B). The biserial seep specimen was oriented with its aperture facing downward, at a
316 ~45° angle from horizontal (Fig. 3A, B). As in the *B. tenuata*, the ultimate (youngest)
317 chamber of this agglutinated individual was less fluorescent, indicating presence of less
318 cytoplasm than in middle chambers (Fig. 3B, C). Mineral grains in the test of the specimen
319 can be discerned in some places (Fig. 3C).
320 The LSCM image of the biserial agglutinant shows it had visible cytoplasmic
321 vacuoles, as well as one large nucleus (Fig. 3C). Compared to the exterior surface of the
322 non-seep specimen's test, this seep specimen lacked an obvious layer of fluorescent material
323 on its test exterior. However, it is clear that short filamentous prokaryotes occurred in
324 sediments in the vicinity of this seep specimen (Fig. 3C). What appears to be either a feeding
325 bolus or reticulopodial trunk is located in the apertural region (Fig. 3C). Because of this
326 specimen's large size, only the older portion of its test was excised and subject to
327 ultrastructural analysis.
328 The TEM micrographs of the agglutinated seep specimen show the presence of large
329 cytoplasmic vacuoles (Fig. 4), most of which lacked preserved membranes. Degradation
330 vacuoles were present (Fig. 4A, B) but not as common as in the non-seep *B. tenuata*
331 specimen. In the space between the organic lining and the interior surface of the test,
332 prokaryotes were sometimes observed (Fig. 4B). There was no evidence of endosymbionts in
333 the endoplasm, although some vacuoles appeared to contain one or two items that appeared to
334 be prokaryotes (Fig. 4A); the identity and role of these microbes is not certain but the reader
335 is directed to the contribution in this issue on prokaryotic associates (e.g., symbionts,
336 parasites; Bernhard et al., this issue). Smaller vacuoles (Fig. 4C, D) appeared to have
337 preserved membranes. Given the slight contrast due to lack of osmication (see above),
338 mitochondria were identified on the basis of size and shape (Fig. 4C, D). In some
339 mitochondria (Fig. 4C, D), a double membrane was clearly noted. The mitochondria did not
340 appear to occur exclusively at the cell periphery. Peroxisomes were noted occasionally in
341 characteristic distributions with endoplasmic reticulum at vacuole peripheries (Fig. 4D;
342 Bernhard and Bowser, 2008); Golgi was also noted (not shown).
343

344 3.1.2 FLEC-TEM Methodological notes

345 Correlative epifluorescence and TEM methods are not novel (e.g., Rieder and Bowser,
346 1987). The FLEC-TEM approach, which was recently described (Bernhard and Richardson,
347 2014), is novel in that it allows examination of cellular attributes in specimens that are
348 located within sediments, where they lived at the time of fixation. The ability to observe the
349 life position of foraminifera, or any other meiofauna, is advantageous to ecological studies
350 but the method does have disadvantages, some of which are discussed in Bernhard and
351 Richardson (2014). Briefly, the disadvantages of FLEC-TEM are: (1) Sectioning of
352 specimens among sediments will expose the diamond knife to heavy use, likely causing
353 damage and the need for resharpening. A novel method that merges use of a focused ion
354 beam (FIB) with the use of a scanning electron microscope (SEM) can produce TEM-quality
355 ultrastructural information in cells (Narayan and Subramaniam, 2015), although this
356 FIB-SEM method has not been performed on foraminifera, to our knowledge. (2) Also, as
357 noted, the lack of osmication prevents preservation and detection of some membranes.
358 Apparent lack of membranes in FLEC-TEM specimens does not necessarily mean the
359 membranes did not exist at the time of fixation. (3) Another disadvantage involves fixation
360 rate. Typically, when materials are preserved in glutaraldehyde, the fixation process is quick
361 because specimens are immersed directly into the fixative solution. With FLEC fixation,
362 however, the fixative must percolate into the sediments contained in the syringe core.
363 Depending on the pore-water content and sediment porosity, as well as specimen location
364 (e.g., deep infaunal vs. epifaunal), fixation of FLEC samples may be considerably slower
365 than immediate fixation of isolated individuals. The slower speed of fixation could impact
366 cellular preservation in unknown ways. (4) Foraminiferal identification at the species or
367 genus level hinges on the plane of section; confident identification can be difficult to
368 impossible. Depending on the study objective(s), such constraints may not be an issue. (5)
369 For some studies, it is imperative to distinguish living from dead specimens (e.g., Bernhard et
370 al., 2010b). Our experience with FLEC-TEM to date indicates that viability in specimens
371 prepared with this method is inconclusive because, for example, mitochondrial status (cristae
372 and double membrane) is not clearly discernable. While significantly degraded cytoplasm is
373 easily detected, any conclusions asserting that a specimen analyzed with FLEC-TEM was
374 living at the time of preservation should be made with due caution.
375
376 3.1.3 Methodological advantages: Merging ecology and physiology

377 Advantages of the FLEC-TEM method include the ability to pair fine-scale
378 distribution with cellular attributes, as described in Bernhard and Richardson (2014) and
379 discussed further below. Because foraminifera move relatively slowly, we expect that the
380 position of individual foraminifera observed in FLEC sections is where the individual lived,
381 unless it was entrained down the core barrel at the edge of the core. Thus, we can distinguish

between surface-living (epifaunal) and deep-dwelling (infaunal) specimens, and we can observe the fitness of each of those cells. In addition to determining position in sediments and orientation of the aperture, FLEC also allows observation about the microhabitat of the individual foraminifer. Thus, the sediment texture, fabric, and pore space can be assessed, as can attributes regarding the neighboring microbial community. If neighbors have distinct morphologies, we can determine if particular types of organisms consistently associate together (Bernhard et al. 2003).

On the cellular scale, FLEC-TEM allows insights regarding adaptations and diet, which can be particularly insightful when considering the fine-scale location of any given individual within sediments, especially in chemoclines where steep geochemical gradients exist. Furthermore, FLEC-TEM can determine if individuals collected from oxygen-depleted environments have specialized features, such as prokaryotic associates, putative symbionts, numerous peroxisomes, or peripheral / pore-plug associated mitochondria.

3.1.4 Observations on the paired ecology and physiology of these seep and non-seep foraminifers

Due to the discernable double membrane and cristae noted in some mitochondria, relatively intact peroxisomes, endoplasmic reticulum and Golgi, as well as abundant degradation vacuoles, and presence of reticulopodial remains on the test exterior (Fig. 2), we assert that the non-seep *Buliminella tenuata* specimen was active (i.e., living) at the time of fixation. Because this specimen was located at a sediment depth of 1.7 cm, the pore-waters bathing this specimen at the time of collection likely were depleted in oxygen (e.g., Bernhard, 1992). There was no evidence of the foraminifer being directly associated with any burrows or tubes, although one tube was present in FLEC sections from the other side of the 1.5-cm diameter FLEC core. Burrows and tubes can oxidize pore waters at depth (e.g., Thibault de Chanvalon et al., 2015). We note that this non-seep *B. tenuata* had mitochondria both at the cell periphery as well as further inside the cell. Foraminifera from low-oxygen habitats often concentrate mitochondria at the cell periphery (e.g., Bernhard et al., 2010a; Leutenegger and Hansen, 1979; see also LeKieffre et al., this issue) but can also have mitochondria throughout the cell. Additional evidence that the specimen was living in oxygen-depleted pore waters is the presence of characteristic peroxisome-endoplasmic reticulum complexes that are often noted in specimens from low-oxygen habitats (Bernhard and Bowser, 2008; see also LeKieffre et al., this issue). The specimen lacked evidence of endosymbionts, which is consistent with the non-seep habitat.

The results presented here on the agglutinated seep foraminifer are valuable because, to our knowledge, observations of the cell ultrastructure and organelle attributes of multi-chambered deep-sea agglutinated foraminifera are not published. This lack of published micrographs likely is because such robust agglutinated tests are extremely challenging to

section.

As with the non-seep *B. tenuata*, assessing viability in the seep-associated biserial agglutinated foraminiferan is difficult. Mitochondria with double membranes and partially discernable cristae were present, as were additional organelles (e.g., peroxisomes, endoplasmic reticulum, small vacuoles with membranes, Golgi), suggesting the specimen was living or recently living. The association of the peroxisomes with the periphery of large vacuoles adds support that this agglutinated foraminifer was living in the seep habitat because, as noted, many foraminifera living in steep chemoclines have such associations (Bernhard and Bowser, 2008; Bernhard et al., 2010b; Martin et al., 2010). The presence of a bolus or reticulopodial trunk in the apertural region (Fig. 3C) provides additional evidence that the agglutinated specimen was active at the time of fixation. The relative dearth of degradation vacuoles suggests the specimen may not have been particularly active at the time of fixation, although it appears that the foraminifer was ingesting prokaryotes (Fig. 4A). It is possible that more degradation vacuoles appeared in the younger part of the specimen that was not examined with TEM.

The seep-associated agglutinated foraminiferan did not appear to be migrating toward the sediment-water interface because its aperture was oriented downward (Fig. 3). Generally, foraminifera move in the direction that their aperture points (e.g., Heinz 1999; H. Nomaki, pers. obs.). Thus, if we assume the specimen was living at the time of fixation, it was not adverse to the localized seep chemistry. Unfortunately, we lack porewater chemical analyses on this specific FLEC core, but the pushcore was collected adjacent to an active chemosynthetic mussel bed. Also, we note presence of some filamentous prokaryotes (Fig. 3C) in the vicinity of the foraminiferan; these filaments could be the sulfide oxidizing *Beggiatoa*, which is commonly known to occur in seeps (e.g., Lloyd et al. 2010).

3.2. Micro-X-ray CT-TEM

3.2.1. Results

The X-ray computed tomography (CT) imaging using the Os- and U-stained foraminifera embedded in resin block showed three-dimensional (3D) structures of foraminiferal cytoplasm (Figs. 5 and 6, Supplementary movies 1, 2, and 3). Using different contrast settings in the software, we were able to observe both external morphology (e.g., Supplementary movie 2) and internal structures larger than several micrometers (e.g., Supplementary movie 3). In a specimen of *Ammonia* sp. (phylotype T6), we observed that the cytoplasm of the ultimate 3 to 5 chambers were less dense in comparison to that of the other chambers based on the differences in X-ray attenuation (Fig. 5A, C, Supplementary movie 1), probably reflecting more vacuoles (Nomaki et al. 2014) and less lipid droplets (Koho et al. this issue), together with less staining of the cytosol (data not shown). Many chambers in the last whorl had relatively large vacuoles (~50 μm in diameter) close to the axis of rotation (Fig.

458 5C). A chamber marked with a white arrowhead in Fig. 5A showed a cytoplasmic depression;
459 this void between the calcite test and cytoplasm is sometimes observed for certain specimens
460 and might be an artifact due to the shrinkage of the cytoplasm during the fixation process. In
461 a specimen of *Bolivina spissa*, the last 2 chambers were "frothy" and not all the chamber
462 space was occupied with cytoplasm (Fig. 6A, B, Supplementary movie 2). The proloculus
463 cytoplasm also looked less dense than other chambers' cytoplasm (Fig. 6C). Cross sectional
464 views showed many vacuoles of 10- to 30-μm diameter throughout all chambers (Fig. 6D, E).
465 Another obvious structure that was observed with micro-X-ray CT is plugs, which had high
466 electron density due to uranium staining (Fig. 6D, Supplementary movie 3; Nomaki et al.
467 2015). Plugs are hypothesized to provide a means to partition portions of the cell not only
468 among different chambers but also into different volumes, which, hypothetically, perform
469 different intracellular biochemical reactions (Hottinger 2000; Ferrández Cañadell 2002).
470 Sometimes, plugs were observed in each chamber of an entire foraminiferal specimen
471 (Nomaki et al. 2015). In some specimens, sediment particles around the aperture and trunks
472 of reticulopods extending from the aperture were also observed (not shown).
473
474 3.2.2. Advantages and applications
475 The advantage of the micro-X-ray CT is to provide an overall view of cytoplasmic
476 conditions, allowing one to target characteristic areas or organelles (e.g., vacuoles, plugs,
477 nucleus). These observations greatly help us to determine the positions of TEM sections. Also,
478 the whole-specimen perspective helps to evaluate the representativeness of the observed
479 ultra-thin section(s) in the observed specimen. Pre-observation of the resin-embedded
480 specimens using micro-X-ray CT before sectioning for TEM observation may become
481 common when micro-X-day CT scanning becomes more affordable and faster.
482 Another advantage of micro-X-ray CT is the ability to quantify the volume or surface
483 area of the region of interest (Nomaki et al. 2015). The volume of cytoplasm in each chamber
484 allows, e.g., calculation of the biovolume, growth pattern through chamber addition, and
485 assessment of fitness. The total cell volume and volume of each vacuole also provides
486 information to estimate the total chemical contents or concentrations in vacuoles. The
487 cytoplasm-occupancy ratio seems to differ greatly between chambers and between species
488 (Figs. 5 and 6, Nomaki et al. 2015), reflecting the volume of vacuoles that might be affected
489 by their environment (LeKieffre et al., this issue).
490
491 3.2.3. Spatial resolution limitations
492 The spatial resolution of the micro-X-ray CT continues to improve; the current spatial
493 resolution of the commercial micro-X-ray CT, e.g. Xradia 410 Versa (ZEISS, this study) or
494 SkyScan 1272 (Bruker; Nomaki et al. 2015), is as low as 0.35 μm. Furthermore, because the
495 differences in X-ray attenuation between metal-labeled cytoplasm and resin are not large as

between calcite (test) and air (e.g., Iwasaki et al. 2015), identification of small organelles like mitochondria and peroxisomes remains difficult. Certain studies using full-field or scanning X-ray microscopes and scanning transmission X-ray microscopes reported 50- or 60-nm resolution of internal fungal features (Larabell and Le Gros 2004; Le Gros et al. 2005), indicating there is potential to observe small organelles in foraminifera. Such high-resolution images, however, can be achieved only for some limited target areas, not for whole foraminiferal cells. High-resolution 3D observations of limited areas are also achieved using a focused ion beam scanning electron microscope (FIB-SEM; e.g., Lucas et al. 2014) technology at a voxel size of 5 to 10 nm with a maximal sample size of 50 × 30 × 30 μm in volume, which remains a small fraction of foraminiferal cell size.

3.3. TEM-NanoSIMS

3.3.1. Elemental and isotope mapping and quantification

Nanometer-scale secondary ion mass spectrometry (NanoSIMS) analyses on a target area of ultra-thin sections or semi-thin sections (Fig. 7A) previously observed with a TEM (Fig. 7B, C) provide qualitative elemental concentration data and stable isotope ratios for imaged and identifiable ultrastructural features (Fig. 7D, E). NanoSIMS $^{12}C^{14}N^-$ ion images contain a wealth of ultrastructural information that enables precise correlation with TEM images (Fig. 7D, E).

An example of isotopic ratio analysis using Look@NanoSIMS showed quantitative information on isotopic compositions of each region of interest (ROI) (Fig. 8). In this example, the foraminifer was fed with ^{13}C-enriched diatoms (d), which were observed with their silica frustules in the foraminiferal endoplasm (Fig. 8A). The ROIs based on the TEM image can be correlated with obtained NanoSIMS images (Fig. 8B, C, D), including isotopic ratios (Fig. 8E), and the quantitative data can be summarized into a table (Fig. 8F).

3.3.2. Examples of 5 different isotope labels

Elemental ratios provide qualitative indications of relative C and N contents in measured areas corresponding to different organelles or ultrastructural features. For example, regions of lipid droplets exhibited lower N concentrations relative to other organelles and the cytosol (Fig. 7D, E). This may reflect low concentrations of N in lipid droplets (and also in the embedding resin), which have been thought to store lipids as a carbon source (LeKieffre et al. 2017, submitted), although the actual contents of “lipid droplets” are not well understood. On the other hand, certain organelles like mitochondria exhibited higher N concentrations than those of the cytosol (Fig. 7D, E; see clearer image in Fig. 2 of Nomaki et al. 2016).

The stable isotopic compositions of C, N, and S, which are calculated with the ratios

of $^{13}C^{12}C^-/^{12}C_2^-$, $^{12}C^{15}N^-/(^{12}C^{14}N^- + ^{12}C^{15}N^-)$ or $^{12}C^{15}N^-/^{12}C^{14}N^-$, and $^{34}S^-/(^{32}S^- + ^{34}S^-)$ or $^{34}S^-/^{32}S^-$, respectively, show the localization of the added stable isotope labels (Fig. 9). For example, the addition of ^{13}C-labeled diatoms revealed the incorporation of food materials (Fig. 9A). While most ^{13}C-labeling was observed within the organic material contained in the diatom frustules, one spot outside a diatom frustule exhibited high ^{13}C-concentrations (lower left of Fig. 9A), suggesting the C in this region was derived from a digested diatom.

The addition of ^{13}C-enriched inorganic C ($H^{13}CO_3^-$) provides information on autotrophic/anaplerotic C fixation into biomass (Fig. 9B). In the example provided in Fig. 9B, foraminifera were supplied with $H^{13}CO_3^-$ to investigate the autotrophic metabolism of kleptoplastic benthic foraminifera. Because soluble ^{13}C-compounds are generally lost from the cell during TEM sample preparation (see section 3.2.4.), the isotope enrichments measured with the NanoSIMS represent 'structural' organic molecules derived from $H^{13}CO_3^-$. This data showed the ^{13}C-assimilated by photosynthetic symbiont and its subsequent transfer and re-processing within the foraminiferal cell.

The assimilation of inorganic sources of ^{15}N (e.g., ammonium or nitrate) can provide an important assessment of nitrogen assimilation and translocation within foraminiferal cells (Fig. 9C, D). Both ammonium and nitrate are important N sources for amino acid synthesis in autotrophic organisms, including foraminiferal symbionts or organelles like kleptoplasts. Here, assimilation of ^{15}N originating from $^{15}NH_4^+$ was observed as small spots of less than 1 μm in diameter, corresponding to electron-opaque bodies (Fig. 9C). Similar assimilation of ^{15}N into electron opaque bodies (called "electron dense bodies" in Nomaki et al. 2016) was also observed in the specimens incubated with $^{15}NO_3^-$ (Fig. 9D). Nitrogen isotopic compositions of amino acids in *Ammonia* sp. (phylotype T6) incubated with $^{15}NO_3^-$ indicated that those ^{15}N labels existed as amino acids probably originated from endobiotic prokaryote (Nomaki et al. 2014; reported as *Ammonia beccarii*). Enrichments in ^{15}N were obvious in electron-opaque bodies of the *Ammonia* sp. (phylotype T6) incubated in anoxia (Fig. 9D), but were also obvious in mitochondria, cytoplasm, and food vacuoles in dysoxia-incubated specimens, suggesting metabolism varied under different oxygen concentrations (Nomaki et al. 2016). Organic lining and lipid droplet regions were modestly labeled with ^{15}N even after 14 days, indicating slower turnover than for other organic matter.

Using $^{34}SO_4^{2-}$ as an isotope tracer in *Ammonia* sp. (phylotype T6) allowed visualization of ^{34}S localization in the cytoplasm (Fig. 9E), likely resulting from metabolism related to sulfur assimilation and/or sulfate reduction by symbionts. Enrichments in ^{34}S were detected in various opaque bodies, but enrichment was also detected in the cytoplasm near vacuoles or as remains inside vacuoles (Fig. 9E). As observed for ^{15}N, ^{34}S assimilation was more pronounced in the specimens incubated with dysoxia versus those incubated in anoxia.

572 3.3.3 Methodological advantages and applications

573 The main advantage of correlated TEM-NanoSIMS observations is the small scale
574 imaging of elements and isotopes. Indeed, this method allows the sub-cellular localization of
575 isotopically labeled compounds, and gives the possibility to quantify isotopic ratios at the
576 scale of organelles (micron to sub-micron scales). Such knowledge has wide applications to
577 studies of foraminiferal biology and physiological processes such as symbiosis, kleptoplasty,
578 trophic metabolism or denitrification. The use of labeled key elements combined with an
579 appropriate incubation time(s) (see below) can also be used to study foraminiferal
580 metabolism under different laboratory-controlled conditions, such as oxic *vs.* dysoxic
581 conditions or light/dark incubations. For instance, symbiosis between ecto-/endobionts or
582 algal symbionts and foraminifera, widely reported in the literature (e.g., Lee and Hallock
583 1987; Lee and Anderson 1991; Bernhard et al. 2000, 2006a, 2010a), are obvious candidates
584 for correlated TEM-NanoSIMS study, because little is known yet about the role of the
585 symbionts or the metabolite transfer between the symbionts and the host cell. For example,
586 phylogenetic studies of *Virgulinella fragilis* endobionts suggest they are putative sulfate
587 reducing δ-proteobacteria (Tsuchiya et al. 2015). The close phylogenetic relationship between
588 the *V. fragilis* endobionts and sulfate reducing δ-proteobacteria suggests these endobionts use
589 organic matter from the host for carbon oxidation. In another example, a study using a
590 radio-isotope tracer in foraminifera containing different algal symbionts suggested that
591 metabolites exchanged between host foraminifera and algal symbionts differed between
592 diatom-retaining foraminifera and dinoflagellate-retaining foraminifera (Kremer et al. 1980).
593 However the Kremer et al. study performed a bulk cell analysis of radio-isotope label transfer,
594 without any spatial information inside the foraminifera. The use of TEM-NanoSIMS with
595 stable isotope labeling could identify the transfer of target elements from specific symbionts
596 to foraminifera or *vice versa* at a sub-micron scale.

597 Time-series sampling in incubation experiments is important for elucidating the actual
598 pathways of the label into foraminiferal ultrastructure or symbiotic partners. For instance, the
599 use of ^{13}C-labeled diatoms as a foraminiferal food source (Figs. 8 and 9A) in a longer
600 incubation reveals the ^{13}C-assimilation into the foraminiferal biomass. The extent of labeling
601 differs between ultrastructural features (i.e., heterogeneity), showing localization in
602 specialized features such as lipid droplets (LeKieffre et al., 2017). Further, prolonged
603 incubations should result in the ^{13}C-label being respired into $^{13}CO_2$ and the ^{13}C-signal in the
604 cytoplasm decreasing over time. The use of NanoSIMS to trace ^{13}C- or ^{15}N-labeled organic
605 matter with appropriate time series sampling, thus has great advantages in metabolic and
606 stoichiometric studies of foraminifera, because one could estimate not only food selectivity
607 but also turnover rates of each organelle type.

608

609 3.3.4. Limitations and challenges

NanoSIMS analysis cannot discriminate which organic molecules were isotopically labeled. Thus, NanoSIMS imaging cannot determine the exact nature of the compounds transferred, but isotope-label localization with ultrastructural observations can provide some guidance. Nevertheless, employing a suite of multiple approaches, such as compound specific isotope analysis of metabolites, genomic and transcriptome analyses, organelle purification with their chemical analyses, in combination with TEM-NanoSIMS, will provide a clearer comprehension of foraminiferal cell metabolism.

Isotopically labeled compounds originally introduced into experiment treatments are not necessarily stable. As incubations proceed over time, labeled substrates can be transformed into other compounds and be available to all entrained organisms in the experimental conditions. Thus the observed isotope-enriched parts in the foraminifera do not necessarily indicate the assimilation of the original labeled compounds, but could indicate the assimilation of other compounds metabolically derived from the original substrates. For example, ammonium or nitrate can be quickly metabolized into ammonium/nitrite/nitrate via microbial processes in the seawater or in sediments (Francis et al. 2007; Libes 2009). Thus the isotope enrichments observed in a long-term experiment requires careful interpretations. Short-term experiments, on the other hand, may be insufficient to label materials for TEM-NanoSIMS analyses that have lower sensitivity than conventional bulk isotope analyses such as EA/IRMS.

Another limitation of the current TEM-NanoSIMS method is that the content of vacuoles and associated soluble compounds in the cytosol (e.g., free amino acids, inorganic carbon, or ions like nitrate and ammonium) are lost during sample preparation. This is unfortunate because these compounds are very important for assessing foraminiferal denitrification, calcification, assimilation and dissimilation processes. Cryofixation of foraminiferal cells (Goldstein and Richardson 2002, this issue) is a potential way to examine those soluble components in the foraminiferal cytosol. Cryofixation is a fixation protocol that preserves a sample with high-pressure freezing at extremely low temperature (Moor 1987). Recently, elemental mapping of the foraminiferal cytoplasm, vesicles and vacuoles using cryofixation reported presence of vacuoles containing calcium in seawater in a cryo-fixed *Amphistegina lobifera* (Khalifa et al, 2016). This is a good example that cryofixation maintains soluble compounds in vacuoles that may be lost during conventional sample preparation protocols. NanoSIMS analyses of cryopreserved specimens should provide more complete information on elemental and isotopic localizations in foraminiferal cells.

From a logistical and resource perspective, TEM-NanoSIMS is a time-consuming method due to sample preparation steps, TEM observation, and isotope mapping using NanoSIMS. Additionally, the instrumentation is costly and can be difficult to access. These facts result in generally low numbers of analyzed TEM-NanoSIMS specimens per experimental condition, hampering generalization of results.

4. Conclusion

The three TEM-related techniques provide a novel perspectives into foraminiferal ecology and biology on different spatial and temporal scales. FLEC-TEM provides sub-millimeter-scale information on foraminiferal life positions and microhabitats in terms of living depth and surrounding milieu including sediment fabric, porosity and meio- and microfaunal communities, all related to foraminiferal ultrastructure and fitness. Micro-X-ray CT-TEM provides 3D views of foraminiferal cells to assess cytoplasmic features such as vacuolization extent to provide volumetric and areal information useful to biomass/biovolume assessments. TEM-NanoSIMS provides micron to nanometer scale information on the distributions of elemental and isotopic compositions in foraminifera along with ultrastructural information, yielding important information about foraminiferal metabolism at the organelle to endobiont scale. Although each of these techniques has limitations, the advantage of correlation with TEM imaging provides different ways to link cell ultrastructures with metabolic processes, ultimately better defining foraminiferal roles in biogeochemical cycling and microbiome ecosystem functioning.

5. Acknowledgments

We thank Ms Kaya Oda (JAMSTEC) for the preparation of the Japanese TEM samples; Katsuyuki Uematsu and Akihiro Tame (Marine Works, Japan) for TEM observations; Akizumi Ishida, Yuji Sano, Naoto Takahata (The University of Tokyo) for NanoSIMS analyses; Chon Chen (JAMSTEC) for help with the onboard sampling of the sediment samples from the bathyal Sagami Bay during the KM16-01 cruise. The electron microscopy platform at the University of Lausanne (Switzerland) is thanked for access and technical assistance. JMB thanks her collaborators Tony Rathburn and Jon Martin on the original seep foraminifera project, Sam Bowser and Sue Goldstein for insightful conversations, Kasia Hammar and Louie Kerr for TEM assistance at the Marine Biological Laboratory (Woods Hole, MA, USA), and the Georgia Electron Microcopy facility at UGA. The comments raised from Prof. Howard Spero and an anonymous reviewer greatly improved our manuscript. This contribution was edited by Prof. Richard Jordan. This work was financially supported by the Grant-in-Aid for Scientific Research from the Ministry of Education, Culture, Sports, Science and Technology, Japan (Scientific Research (C) grant number 17K05697 to HN) and the Swiss National Science Foundation (grant no. 200021_149333). JMB's contributions were funded by US NSF grants OCE-0551001 and OCE-1634469, the WHOI Robert W. Morse Chair for Excellence in Oceanography, and The Investment in Science Fund at WHOI. The micro-X-ray CT imaging was performed under the cooperative research program of Center for Advanced Marine Core Research (CMCR), Kochi

University (accept No. 17A021).

6. References

Alexander, S.P., Banner, F.T., 1984. The functional relationship between skeleton and cytoplasm in *Haynesina germanica* (Ehrenberg). J. Foramin. Res. 14, 159–170.

Alve, E., Bernhard, J. M., 1995. Vertical migratory response of benthic foraminifera to controlled oxygen concentrations in an experimental mesocosm. Mar. Ecol. Prog. Ser. 116, 137–151.

Bernhard, J.M., 1992. Benthic foraminiferal distribution and biomass related to pore-water oxygen content- Central California Continental Slope and Rise. Deep-Sea Res. 39 (3-4A), 585–605.

Bernhard, J. M., 2003. Potential symbionts in bathyal foraminifera. Science 299, 861. doi: 10.1126/science.1077314

Bernhard, J.M., Bowser, S.S., 1996. Novel epifluorescence microscopy method to determine life position of foraminifera in sediments. J. Micropalaeontol. 15, 68.

Bernhard, J. M., Bowser. S. S., 2008. Peroxisome proliferation in foraminifera inhabiting the chemocline: an adaptation to reactive oxygen species exposure? J. Eukaryot. Microbiol. 55, 135–144 doi: 10.1111/j.1550-7408.2008.00318.x

Bernhard, J. M., Richardson, E. A., 2014. FLEC-TEM: Using microscopy to correlate ultrastructure with life position of infaunal foraminifera. In Approaches to Study Living Foraminifera: Collection, Maintenance and Experimentation. [Kitazato, H. Bernhard, J. M. eds] Springer Japan

Bernhard, J. M., Buck, K. R., Farmer, M. A., Bowser, S. S., 2000. The Santa Barbara Basin is a symbiosis oasis. Nature 403, 77–80, doi:10.1038/47476

Bernhard, J. M., Buck, K. R., Barry, J. P., 2001. Monterey Bay cold-seep biota: Assemblages, abundance, and ultrastructure of living foraminifera. Deep-Sea Res. PT I 48 (10), 2233–2249. doi: 10.1016/S0967-0637(01)00017-6

Bernhard, J. M., Visscher, P. T., Bowser, S. S., 2003. Submillimeter life positions of bacteria, protists, and metazoans in laminated sediments of the Santa Barbara Basin. Limnol. Oceanogr. 48 (2), 813–828. doi: 10.4319/lo.2003.48.2.0813

Bernhard, J. M., Habura, A., Bowser, S. S., 2006a. An endobiont-bearing allogromiid from the Santa Barbara Basin: Implications for the early diversification of foraminifera. J. Geophys. Res. 111, G03002, doi:10.1029/2005JG000158

Bernhard, J. M., Ostermann, D. R., Williams, D. S., Blanks, J. K., 2006b. Comparison of two methods to identify live benthic foraminifera: A test between Rose Bengal and CellTracker Green with implications for stable isotope paleoreconstructions. Paleoceanography 21, PA4210, doi:10.1029/2006PA001290

723 Bernhard, J. M., Barry, J. P., Buck, K. R., Starczak, V. R., 2009. Impact of intentionally
724 injected carbon dioxide hydrate on deep-sea benthic foraminiferal survival. Glob.
725 Change Biol. 15:2078–2088. doi: 10.1111/j.1365-2486.2008.01822.x
726 Bernhard, J. M., Goldstein, S. T., Bowser, S. S., 2010a. An ectobiont-bearing foraminiferan,
727 *Bolivina pacifica*, that inhabits microxic pore waters: cell-biological and
728 paleoceanographic insights. Environ. Microbiol. 12, 2107–2119
729 doi:10.1111/j.1462-2920.2009.02073.x
730 Bernhard, J. M., Martin, J. B., Rathburn, A. E., 2010b. Combined carbonate carbon isotopic
731 and cellular ultrastructural studies of individual benthic foraminifera: 2. Toward an
732 understanding of apparent disequilibrium in hydrocarbon seeps. Paleoceanography 25,
733 PA4206, doi:10.1029/2010PA001930
734 Bernhard, J. M., Edgcomb, V. P., Visscher, P. T., McIntyre-Wressnig, A., Summons, R.,
735 Bouxsein, M. L., Louis, L., Jeglinski, M., 2013. Insights into foraminiferal influences
736 on microfabrics of microbialites at Highborne Cay, Bahamas. Proc. Natl Acad. Sci.
737 USA 110, 9830–9834. doi: 10.1073/pnas.1221721110
738 Briguglio, A., Metscher, B., Hohenegger, J., 2011. Growth rate biometric quantification by
739 X-ray microtomography on larger benthic foraminifera: three-dimensional
740 measurements push nummulitids into the fourth dimension. Turkish J. Earth Sci. 20,
741 683-699. doi:10.3906/yer-0910–44
742 Briguglio, A, Hohenegger, J., Less, G., 2013. Paleobiological applications of
743 three-dimensional biometry on larger benthic foraminifera: a new route of discoveries.
744 J. Foramin. Res. 43, 72–87. doi: 10.2113/gsjfr.43.1.72
745 Carpenter, K. J., Weber, P. K., Lee Davisson, M., Pett-Ridge, J., Haverty, M. I., Keeling, P.J.,
746 2013. Correlated SEM, FIB-SEM, TEM, and NanoSIMS imaging of microbes from
747 the hindgut of a lower termite: methods for *in situ* functional and ecological studies of
748 uncultivable microbes. Microsc. Microanal. 19, 1490–1501. doi:
749 10.1017/S1431927613013482
750 Dahlgren, L., 1967a. On the ultrastructure of the gamontic nucleus and the adjacent
751 cytoplasm of the monothalamous foraminifer *Ovammina opaca* Dahlgren. Zool.
752 Bidrag, Uppsala Bd 37, 77–112.
753 Dahlgren, L., 1967b. On the nuclear distribution of RNA and DNA and on the ultrastructure
754 of nuclei and adjacent cytoplasm of the foraminifers *Hippocrepinella alba*
755 Heron-Allen and Earland *Globobulimina turgida* (Bailey). Zool. Bidrag, Uppsala Bd
756 37, 113–138.
757 Ferrández Cañadell, C., 2002. Multicellular-like compartmentalization of cytoplast in fossil
758 larger foraminifera. Lethaia 35, 121–130 doi: 10.1111/j.1502-3931.2002.tb00073.x
759 Ferrández Cañadell, C., Briguglio, A., Hohenegger, J., Woger, J., 2014. Test fusion in adult
760 foraminifera: A review with new observations of an Early Eocene *Nummulites*

761 specimen. J. Foramin. Res. 44, 316–324 doi: 10.2113/gsjfr.44.3.316
762 Finzi-Hart, J. A., Pett-Ridge, J., Weber, P. K., Popa, R., Fallon, S. J., Gunderson, T., Hutcheon,
763 I. D., Nealson, K. H., Capone, D. G., 2009. Fixation and fate of C and N in the
764 cyanobacterium *Trichodesmium* using nanometer-scale secondary ion mass
765 spectrometry. Proc. Natl Acad. Sci. USA 106, 6345–6350. doi:
766 10.1073/pnas.0810547106
767 Francis, C. A., Beman, J. M., Kuypers, M. M. M., 2007. New processes and players in the
768 nitrogen cycle: the microbial ecology of anaerobic and archaeal ammonia oxidation.
769 The ISME J. 1, 19–27. doi:10.1038/ismej.2007.8
770 Geslin, E., Heinz P., Hemleben, C., Jorissen, F. J., 2004. Migratory response of deep-sea
771 benthic foraminifera to variable oxygen conditions: laboratory investigations. Mar.
772 Micropaleontol. 53: 227–243. doi: 10.1016/j.marmicro.2004.05.010
773 Glud, R. N., Wenzhoefer, F., Tengberg, A., Middelboe, M., Oguri, K., Kitazato, H., 2005.
774 Distribution of oxygen in surface sediments from central Sagami Bay, Japan: In situ
775 measurements by microelectrodes and planar optodes. Deep-Sea Res. PT I, 52,
776 1974–1987 doi:10.1016/j.dsr.2005.05.004
777 Glud, R. N., Thamdrup, B., Stahl, H., Wenzhoefer, F., Glud, A., Nomaki, H., Oguri, K.,
778 Revsbech, N. P., Kitazato, H., 2009. Nitrogen cycling in a deep ocean margin
779 sediment (Sagami Bay, Japan). Limnol. Oceanogr. 54, 723–734 doi:
780 10.4319/lo.2009.54.3.0723
781 Goldstein, S. T., Richardson, A. E., 2002. Comparison of test and cell body ultrastructure in
782 three modern allogromiid foraminifera: application of high pressure freezing and
783 freeze substitution. J. Foramin. Res. 32, 375–383.
784 Goldstein, S. T., Richardson, A. E., submitted. Fine structure of the foraminifer *Haynesina*
785 *germanica* (Ehrenberg) and its sequestered chloroplasts. Mar. Micropaleontol.
786 Gross, O., 2000. Influence of temperature, oxygen and food availability on the migrational
787 activity of bathyal benthic foraminifera: evidence by microcosm experiments.
788 Hydrobiologia. 426, 123–137.
789 Hanaichi, T., Sato, T., Iwamoto, T., Malavasi-yamashiro, J., Hoshino, M., Mizuno, N., 1986.
790 A stable lead by modification of Sato method. J. Electron. Microsc. 35, 304–306.
791 Hayat, M. A., 2000. Principals and techniques of electron microscopy: biological applications
792 (4th edition). 564pp. Cambridge University Press, Cambridge, UK.
793 Hayward, B. W., Holzmann, M., Grenfell, H. R., Pawlowski, J., Triggs, C. M., 2004.
794 Morphological distinction of molecular types in *Ammonia* - towards a taxonomic
795 revision of the world's most commonly misidentified foraminifera. Mar.
796 Micropaleontol. 50, 237–271.
797 Hedley, R. H., Parry, D. M., Wakefield, J. St. J., 1967. Fine structure of *Sphepheardella*
798 *taeniformis* (Foraminifera; Protozoa). J. R. Microsc. Soc. 87, 445–456.

Heinz, P. 1999. Response of deep-sea benthic foraminifera to simulated phytodetritus pulses under laboratory conditions. Tübinger Mikropaläontologische Mitteilungen 20, 126 pp., Tübingen.

Heinz, P., Kitazato, H., Schmiedl, G., Hemleben, C., 2001. Response of deep-sea benthic foraminifera from the Mediterranean Sea to simulated phytoplankton pulses under laboratory conditions. J. Foramin. Res. 31, 210–227.

Hohenegger, J., Briguglio, A., 2012. Axially oriented sections of nummulitids: a tool to interpret larger benthic foraminiferal deposits. J. Foramin. Res. 42, 145–153. doi:10.2113/gsjfr.42.2.134

Holzmann, M., 2000. Species concept in foraminifera: *Ammonia* as a case study. Micropaleontology 46, 21–37.

Hoppe, P., Cohen, S., Meibom, A., 2013. NanoSIMS: Technical aspects and applications in cosmochemistry and biological geochemistry. Geostand. Geoanal. Res. 37:111–154. doi: 10.1111/j.1751-908X.2013.00239.x

Hottinger, L., 2000. Functional morphology of benthic foraminiferal shells, envelopes of cells beyond measure. Micropaleontology 46 (suppl 1), 57–86.

Iwasaki, S., Kimoto, K., Sasaki, O., Kano, H., Honda, M. C., Okazaki, Y., 2015. Observation of the dissolution process of *Globigerina bulloides* tests (planktic foraminifera) by X-ray microcomputed tomography. Paleoceanography 30, 317–331. doi: 10.1002/2014PA002639

Jauffrais, T., Jesus, B., Metzger, E., Mouget, J. L., Jorissen, F., Geslin, E., 2016. Effect of light on photosynthetic efficiency of sequestered chloroplasts in intertidal benthic foraminifera (*Haynesina germanica* and *Ammonia tepida*). Biogeosciences. 13, 2715–2726. doi:10.5194/bg-13-2715-2016

Jauffrais, T., Jesus, B., Meleder, V., Geslin E., 2017. Functional xanthophyll cycle and pigment content of a kleptoplastic benthic foraminifer: *Haynesina germanica*. PLoS ONE 12: e0172678. doi:10.1371/journal.pone.0172678

Johnstone, H. J. H., M. Schulz, S. Barker, Elderfield, H., 2010. Inside story: An X-ray computed tomography method for assessing dissolution in the tests of planktonic foraminifera. Mar. Micropaleontol., 77, 58–70. doi:10.1016/j.marmicro.2010.07.004

Jorissen, F. J., de Stigter, H. C., Widmark, J. G. V., 1995. A conceptual model explaining benthic foraminiferal microhabitats. Mar. Micropaleontol. 26, 3–15.

Khalifa, G. M., Kirchenbuechler, D., Koifman, N., Kleinerman, O., Talmon, Y., Elbaum, M., Addadi, L., Weiner, S., Erez, J., 2016. Biomineralization pathways in a foraminifer revealed using a novel correlative cryo-fluorescence-SEM-EDS technique. J Struct Biol. 196, 155–163. doi: 10.1016/j.jsb.2016.01.015.

Koho, K. A., Piña-Ochoa, E., Geslin, E., Risgaard-Petersen, N., 2011. Vertical migration, nitrate uptake and denitrification: Survival mechanisms of foraminifers

(*Globobulimina turgida*) under low oxygen conditions. FEMS Microbiol. Ecol. 75, 273–283, doi:10.1111/j.1574-6941.2010.01010.x

Koho, K. A., LeKieffre, C., Nomaki, H., Salonen, I., Geslin, E., Mabilleau, G., Jensen, L. H. S., Reichart, G. J., in revision. Changes in ultrastructural features of the foraminifera *Ammonia* spp. in response to anoxic conditions: field and laboratory observations. Mar. Micropaleontol. This issue.

Kopp, C., Domart-Coulon, I., Escrig, S., Humbel, B. M., Hignette, M., Meibom, A., 2015. Subcellular investigation of photosynthesis-driven carbon assimilation in the symbiotic reef coral *Pocillopora damicornis*. mBio 6, e02299-14. doi:10.1128/mBio.02299-14.

Kremer, B. P., Schmaljohann, R., Röttger, R., 1980. Features and nutritional significance of photosynthates produced by unicellular algae symbiotic with larger foraminifera. Mar. Ecol. Prog. Ser, 2, 225–228.

Larabell, C. A., Le Gros, M. A., 2004. X-ray tomography generates 3-D reconstructions of the yeast, *Saccharomyces cerevisiae*, at 60-nm resolution. Mol. Biol. Cell 15:957–962 doi:10.1091/mbc.E03–07–0522

Lee, J. J. Hallock, P., 1987. Algal symbiosis as the driving force in the evolution of larger foraminifera. Ann. N. Y. Acad. Sci. 503, 330–347, doi: 10.1111/j.1749-6632.1987.tb40619.x

Lee, J. J., Anderson O. R., 1991. Symbiosis in Foraminifera, p.157–220. In J. J. Lee and O. R. Anderson [eds.], Biology of Foraminifera. Academic Press.

Le Gros, M. A., McDermott, G., Larabell, C. A., 2005. X-ray tomography of whole cells. Curr. Opin. Struc. Biol. 15: 593–600 doi:10.1016/j.sbi.2005.08.008

LeKieffre, C., Spangenberg, J. E., Mabilleau, G., Escrig, S., Meibom, A., Geslin, E., 2017. Surviving anoxia in marine sediments: The metabolic response of ubiquitous benthic foraminifera (*Ammonia tepida*). PLoS ONE. 12(5): e0177604. doi: 10.1371/journal.pone.0177604

LeKieffre, C., Bernhard, J. M., Mabilleau, G., Filipsson, H. L., Meibom, A., Geslin, E., submitted. An overview of cellular ultrastructure in benthic foraminifera: New observations in the context of existing literature. Mar. Micropal.

Leutenegger, S., Hansen, H. J., 1979. Ultrastructural and Radiotracer studies of pore function in foraminifera. Mar. Biol. 54, 11–16.

Libes, S. M., 2009. *Introduction to marine biogeochemistry, 2nd edition*. Academic Press.

Lucas, M. S., Guenthert, M., Gasser, P., Lucas, F., Wepf, R., 2014. Correlative 3D imaging: CLSM and FIB-SEM tomography using high-pressure frozen, freeze-substituted biological samples. Methods Mol. Biol. 1117:593–616. doi: 10.1007/978-1-62703-776-1_26

Lloyd, K. G., Albert, D. B., Biddle, J. F., Chanton, J. P., Pizarro, O., Teske, A., 2010. Spatial

875 structure and activity of sedimentary microbial communities underlying a *Beggiatoa*
876 spp. mat in a Gulf of Mexico hydrocarbon seep. PLoS ONE 5(1): e8738.
877 doi:10.1371/journal.pone.0008738
878 Martin, J. B., Bernhard, J. M., Curtis, J., Rathburn, A. E., 2010. Combined carbonate carbon
879 isotopic and cellular ultrastructural studies of individual benthic foraminifera: Method
880 description. Paleoceanography 25, PA2211, doi:10.1029/2009PA001846
881 Metzger, E., Thibault de Chanvalon, A., Cesbron, F., Barbe, A., Launeau, P., Jézéquel, D.,
882 Mouret, A., 2016. Simultaneous nitrite/nitrate imagery at millimeter scale through the
883 water-sediment interface. Environ. Sci. Technol. 50, 8188–8195. doi:
884 10.1021/acs.est.6b00187
885 Micheva, K. D., Smith, S. J., 2007. Array tomography: a new tool for imaging the molecular
886 architecture and ultrastructure of neural circuits. Neuron 55, 25–36.
887 doi:10.1016/j.neuron.2007.06.014
888 Moodley, L., van der Zwaan, G. J., Rutten, G. M. W., Boom, R. C. E, Kempers, A. J., 1998.
889 Subsurface activity of benthic foraminifera in relation to porewater oxygen content:
890 laboratory experiments. Mar. Micropaleontol. 34, 91–106.
891 Moor, H., 1987. Theory and practice of high pressure freezing. *In* Cryotechniques in
892 Biological Electron Microscopy [Steinbrecht, R. A., Zierold, K. eds.] Springer-Verlag,
893 Berlin, p. 175–191.
894 Murray, J. W., 1996. Ecology and Applications of Benthic Foraminifera. Cambridge
895 University Press.
896 Musat, N., Stryhanyuk, H., Bombach, P., Adrian, L., Audinot, J.-N., Richnow, H. H., 2014.
897 The effect of FISH and CARD-FISH on the isotopic composition of ^{13}C- and
898 ^{15}N-labeled *Pseudomonas putida* cells measured by nanoSIMS. Syst. Appl. Microbiol.
899 37, 267–276. doi:10.1016/j.syapm.2014.02.002
900 Narayan, K., Subramaniam, S., 2015. Focused ion beams in biology. Nature Methods 12 (11),
901 1021-1031. doi:10.1038/nmeth.3623
902 Nomaki, H., Heinz, P., Hemleben, C., Kitazato, H., 2005. Behaviors and responses of
903 deep-sea benthic foraminifera to freshly supplied organic matter: Laboratory feeding
904 experiments in microcosm environments. J. Foramin. Res. 35, 103–113. doi:
905 10.2113/35.2.103
906 Nomaki, H., Chikaraishi, Y., Tsuchiya, M., Toyofuku, T., Ohkouchi, N., Uematsu, K., Tame,
907 A., Kitazato, H., 2014. Nitrate uptake by foraminifera and use in conjunction with
908 endobionts under anoxic conditions. Limnol. Oceanogr. 59, 1879–1888. doi:
909 10.4319/lo.2014.59.6.1879
910 Nomaki, H., Toyofuku, T., Tsuchiya, M., Matsuzaki, T., Uematsu, K., Tame, A., 2015.
911 Three-dimensional observation of foraminiferal cytoplasmic morphology and internal
912 structures using uranium–osmium staining and micro-X-ray computed tomography.

913 Mar. Micropaleontol. 121, 32–40. doi:10.1016/j.marmicro.2015.09.003
914 Nomaki, H., Bernhard, J. M., Ishida, A., Tsuchiya, M., Uematsu, K., Tame, A., Kitahashi, T.,
915 Takahata, N., Sano, Y., Toyofuku, T., 2016. Intracellular isotope localization in
916 *Ammonia* sp. (Foraminifera) of oxygen-depleted environments: results of nitrate and
917 sulfate labeling experiments. Front. Microbiol., 7, Article 163, doi:
918 10.3389/fmicb.2016.00163
919 Pernice, M., Meibom, A., Van Den Heuvel, A., Kopp, C., Domart-Coulon, I.,
920 Hoegh-Guldberg, O., Dove, S., 2012. A single-cell view of ammonium assimilation in
921 coral-dinoflagellate symbiosis. The ISME J., 6, 1314–1324.
922 Polerecky, L., Adam, B., Milucka, J., Musat, N., Vagner, T., Kuypers, M. M. M., 2012.
923 Look@NanoSIMS – a tool for the analysis of nanoSIMS data in environmental
924 microbiology. Environ. Microbiol. 14, 1009–1023.
925 doi:10.1111/j.1462-2920.2011.02681.x
926 Rieder, C. L., Bowser, S. S., 1987. Correlative light and electron microscopy on the same
927 epoxy section. In: Hayat, M.A. (Ed.), Correlative Microscopy in Biology:
928 Instrumentation and Methods. Academic Press, Orlando, pp. 249-277.
929 Speijer, R. P., Loo, D. V., Masschaele, B., Vlassenbroeck, J., Cnuddle, V., Jacobs, P., 2008.
930 Quantifying foraminiferal growth with high-resolution X-ray computed tomography:
931 New opportunities in foraminiferal ontogeny, phylogeny, and paleoceanographic
932 applications. Geosphere 4, 760–763. doi:10.1130/GES00176.1
933 Thibault de Chanvalon, A., Metzger, E., Mouret, A., Cesbron, F., Knoery, J., Rozuel, E.,
934 Launeau, P., Nardelli, M. P., Jorissen, F. J., Geslin, E., 2015. Two-dimensional
935 distribution of living benthic foraminifera in anoxic sediment layers of an estuarine
936 mudflat (Loire estuary, France). Biogeosciences, 12, 6219–6234.
937 doi:10.5194/bg-12-6219-2015
938 Travis, J. L., Bowser, S. S., 1986. A new model of reticulopodial motility and shape:
939 Evidence for a microtubule-based motor and an actin skeleton. Cell. Motil.
940 Cytoskeleton 6, 2–14.
941 Tsuchiya, M., Toyofuku, T., Uematsu, K., Bruchert, V., Collen, J., Yamamoto, H., Kitazato,
942 H., 2015. Cytologic and genetic characteristics of endobiotic bacteria and kleptoplasts
943 of *Virgulinella fragilis* (Foraminifera). J. Eukaryot. Microbiol. 62, 454–469.
944 doi:10.1111/jeu.12200
945 Yabuki, A., Chao, E. E., Ishida, K., Cavalier-Smith, T., 2012. *Microheliella maris*
946 (Microhelida ord. n.), an ultrastructurally highly distinctive new axopodial protist
947 species and genus, and the unity of phylum Heliozoa. Protist 163, 356–388.
948 doi:10.1016/j.protis.2011.10.001

949 Yabuki, A., Eikrem, W., Takishita, K., Patterson, D. J., 2013. Fine structure of *Telonema*
950 *subtilis* Griessmann, 1913: A flagellate with a unique cytoskeletal structure among
951 eukaryotes. Protist 164, 556–569. doi:10.1016/j.protis.2013.04.004
952
953
954

955
956 **Figure legends**
957
958 **Figure 1 (view in color)**. Light micrographs of *Buliminella tenuata* in living position in
959 non-seep sediments. A. Reflected light image showing excised portion of FLEC section that
960 includes the foraminifer (white arrowhead). The black marking (white ^) is a permanent
961 marker to guide in locating the specimen during excision. Note that the top of the sediment in
962 the image is not the sediment-seawater interface (see text). B. LSCM micrograph showing
963 the fluorescent specimen in sediments. Note the vacuolated nature of the cytoplasm,
964 relatively empty ultimate chamber and veil of fluorescent material on the test exterior (arrows).
965 sg1 and sg2 mark particular sediment grains that are also visible in C. C. Transmitted light
966 micrograph of a thick section stained with toluidine blue, showing the specimen after
967 sectioning. Note the holes where the sediment grains (sg1, sg2) occurred. t = test. * = open
968 pore space adjacent to aperture. Scales: A = 500 µm; B, C = 100 µm.
969
970 **Figure 2**. Transmission electron micrographs of *B. tenuata* collected from non-seep
971 sediments. A. Overview of chamber periphery showing cytoplasm with large vacuoles (v) and
972 degradation vacuoles (dv). po = pores; t = location of former test; white arrowhead =
973 prokaryote in degradation vacuole. B. Internal edge of chamber showing mitochondria (m)
974 and degradation vacuoles. g = Golgi. C. Periphery of chamber, tangentially through pores,
975 showing mitochondria associated with pores and Golgi. ol= organic lining; eo=
976 electron-opaque body; black arrow = mitochondrial double membrane. Inset: cross section
977 through pore showing preservation of fibrous material. D. Chamber periphery showing
978 mitochondria and Golgi. E. Peroxisomes (p) complexed with endoplasmic reticulum (er),
979 showing darker core (inset). F,G. Images taken outside the foraminiferan test, which existed
980 in the light-colored spaces. Areas of interest are the blebs (*), which likely were reticulopods
981 that produced the fluorescence on the test exterior in Fig. 1B. Scales: A = 2 µm; B,G = 1 µm;
982 C-F = 0.5 µm.
983
984 **Figure 3 (view in color)**. Light micrographs of an agglutinated biserial foraminifer in living
985 position in seep sediments. A, B. Paired images showing specimens in life position in
986 sediments preserved with FLEC. A. Double exposure micrograph of epifluorescence and
987 reflected light showing foraminifer in life position 1.3 mm below the sediment-water interface
988 and close to a juvenile bivalve (+). White and black arrow = cross section of a calcareous
989 foraminifer. B. Epifluorescence micrograph revealing microbes (fluorescent items including
990 prokaryotes and/or eukaryotes; some are labeled with white arrowheads) shown in this image.
991 Note the calcareous foraminifer noted in A is not fluorescent (i.e., dead). C. LSCM micrograph
992 showing the vacuolated nature of the cytoplasm, nucleus (black *), relatively empty ultimate

(youngest) chamber (#), feeding bolus or reticulopodial trunk near the aperture (white arrow), and mineral grains in test (white *). Note the fine filaments in the adjacent sediments (white arrowheads). t = test. Scales: B = 1 mm (A = same magnification as B); C = 200 μm.

Figure 4. Transmission Electron Micrographs of a biserial agglutinated foraminifer collected from seep sediments. A. Overview, including portion of cell periphery with organic lining (ol), showing cytoplasm with large empty vacuoles (v) and some appearing to include 1-2 prokaryotes (black arrows) and digestive vacuoles (dv). Fractured mineral grains from test (t) are evident; empty (white) space is space formerly occupied by sediment grains (i.e., foraminiferal test). B. Overview showing prokaryotes (arrows) occurring in the lumen between organic lining and interior surface of test. C. Area showing what are interpreted to be mitochondria (m), along with vacuoles and organic lining. Some mitochondria have faintly visible double membranes (white arrowhead). D. More mitochondria with faint double membranes and cristae (white arrowheads), along with peroxisomes (p) and endoplasmic reticulum (er). Scales: A,B = 2 μm; C = 1 μm; D = 0.5 μm.

Figure 5 (view in color). Micro-X-ray CT slice images of *Ammonia* sp. (phylotype T6) incubated under dysoxic condition. A. Reconstructed micro-X-ray CT image of the *Ammonia* sp. White arrowhead shows a depressed cytoplasm in the chamber. B. Cross-sectional view of the CT image indicated as b1'-b2' to b1"-b" in A. C. A cross-sectional view from the spiral side. D. A cross-sectional view of the CT image indicated as d1'-d2' to d1"-d2" in A. In the panels B, C, and D, white indicates more X-ray absorbance, meaning higher electron density. Note that this specimen was sectioned for TEM observation before carrying out the micro-X-ray CT imaging. Scale bars = 100 μm.

Figure 6 (view in color). Micro-X-ray images of *Bolivina spissa* collected from the bathyal Sagami Bay. A. Reconstructed micro-X-ray CT image of the *Bolivina spissa*. B. A view from the aperture side indicated as the arrow b in A. C. A view from the proloculus side indicated as the arrow c in A. D. A cross-sectional view of the *Bolivina spissa* indicated as the plane d in A. Many vacuoles (v) and a part of plug (pl) are visible. E. A cross-sectional view of the *Bolivina spissa* indicated as the plane e in A. In panels D and E, white indicates more X-ray absorbance, meaning higher electron density. Scale bars = 100 μm.

Figure 7 (view in color). Examples of TEM-NanoSIMS analysis on *Ammonia* sp. (phylotype T6) incubated under dysoxic conditions. A. Osmium coated semi-thin sections of *Ammonia* sp. (phylotype T6) on a copper grid. Note that the TEM observations (B, C, D, and E) were carried out before the osmium coating. B. Low-magnification TEM image of the whole specimen. The square marked with c indicate the area where montage images of TEM were

made. C. Montage images of TEM which were observed with ×3,500 magnification. The squares marked with d and e indicate the area where NanoSIMS analysis were performed. D and E. Correlative TEM images and NanoSIMS images on nitrogen mapping ($^{12}C^{14}N^-$ count per each pixel) and the ratio of $^{15}N/^{14}N$ ($^{12}C^{15}N^-$ count /$^{12}C^{14}N^-$ count per each pixel). m: mitochondria, li: lipid droplet, v: vacuole. D: 15 µm x 15 µm. E: 12 µm x 12 µm.

Figure 8 (view in color). Isotopic signal quantification on NanoSIMS images with the software Look@NanoSIMS (Polerecky et al., 2012). The example illustrated in this figure is a quantification of the $\delta^{13}C$ in the endoplasm of a species of *Ammonia* sp. (phylotype T6) which was fed with ^{13}C-enriched diatoms. A: TEM micrograph of the endoplasm of an *Ammonia* sp. (phylotype T6) B: Corresponding $^{12}C^{14}N$ NanoSIMS image. C: Overlay of the TEM and $^{12}C^{14}N$ NanoSIMS images following the alignment procedure with the software Look@NanoSIMS; blue: TEM, red: $^{12}C^{14}N$ image. D: Drawing of regions on interest (ROIs) on the overlay image (here the ROIs are diatoms). The ROIs are numbered order from left to right. E: Application of the ROI template on the aligned $\delta^{13}C$ NanoSIMS image. F: Results compiled in a table by the software, each line corresponds to one ROI: identification (#i), positions x and y of the ROI central point (Xi and Yi), $\delta^{13}C$ enrichment value (MEANi, here in ‰), Poisson error (Poiss_Ei, theoretical precision of the mean), size: diameter in µm (SIZESi) and in pixels (PIXELSi), and classification (here “d” for diatom). d: diatom. Scale bars: 5 µm.

Figure 9 (view in color). TEM micrographs (left) and corresponding NanoSIMS images (right) of the endoplasm of different foraminiferal species incubated with different sources of isotopes. A. *Ammonia* sp. (phylotype T6) fed with a ^{13}C-enriched diatom biofilm. The ^{13}C signal could be traced in the diatoms ingested inside the foraminiferal endoplasm (for more details see LeKieffre et al. in press). B. *Haynesina germanica* incubated with $H^{13}CO_3^-$ as a source of inorganic carbon. C. *Nonionellina labradorica* incubated with $^{15}NH_4^+$ as a source of inorganic nitrogen. D. *Ammonia* sp. (phylotype T6) incubated with $^{15}NO_3^-$ as a source of inorganic nitrogen in anoxia. E. *Ammonia* sp. (phylotype T6) incubated with $^{34}SO_4^{3-}$ as a source of inorganic sulfur in dysoxia. White arrowheads indicate the labeled isotope localization in the foraminiferal cytoplasm and the black arrowheads indicate the corresponding region in the TEM images. d: diatom, n: nucleus, v: vacuole, c: chloroplast, m: mitochondria, ob: electron opaque body, eb: elongated body, dv: degradation vacuole.

Supplementary movie 1. Reconstructed 3-D micro-X-ray CT image of *Ammonia* sp. (phylotype T6), obtained with the Xradia 410 Versa microfocus X-ray CT system. Note that this specimen was sectioned for TEM observation before conducting micro-X-ray CT imaging. The ultimate 3 to 4 chambers look frothy (less densely packed) in comparison to

other chambers. Among the ultimate 3 to 4 chambers, the outer portions of the chambers appear denser than the inner portions (closest to the axis of rotation), reflecting what appears to be more vacuoles nearer the aperture of this species. Particles showing high X-ray attenuation are (mineral) particles originally attached on the umbilical part outside the calcite test.

Supplementary movie 2. Reconstructed 3-D micro-X-ray CT image of *Bolivina spissa*, obtained with the Xradia 410 Versa microfocus X-ray CT system, showing external surface of the cytosol, together with large vacuoles.

Supplementary movie 3. Reconstructed 3-D micro-X-ray CT image of the same *Bolivina spissa* specimen in Supplementary movie 2, but the obtained image was processed to visualize the inner structure. In the cross section, plugs separating cytoplasm between chambers, shown in red (high densities), were clearly observed through the entire cross section. Note that the color contrast was altered from Supplementary movie 2 to better illustrate the plugs.

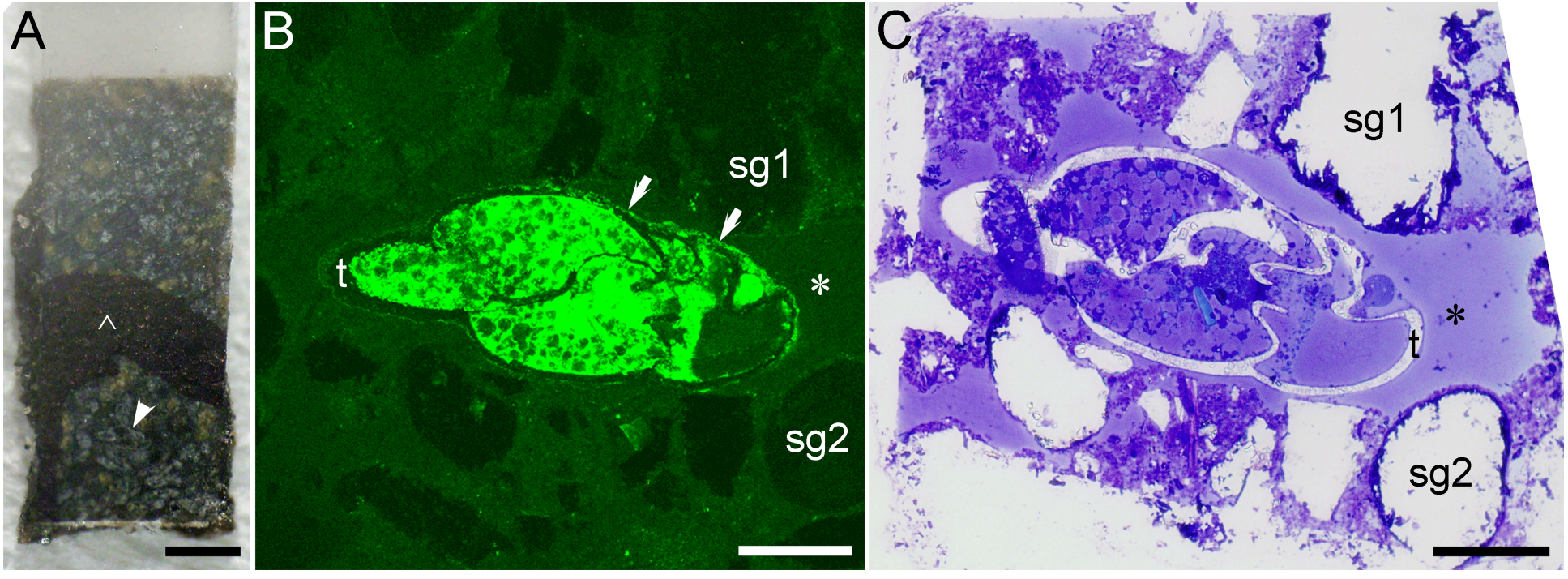
A
B
sg1
t
*
sg2
C
sg1
t
*
sg2

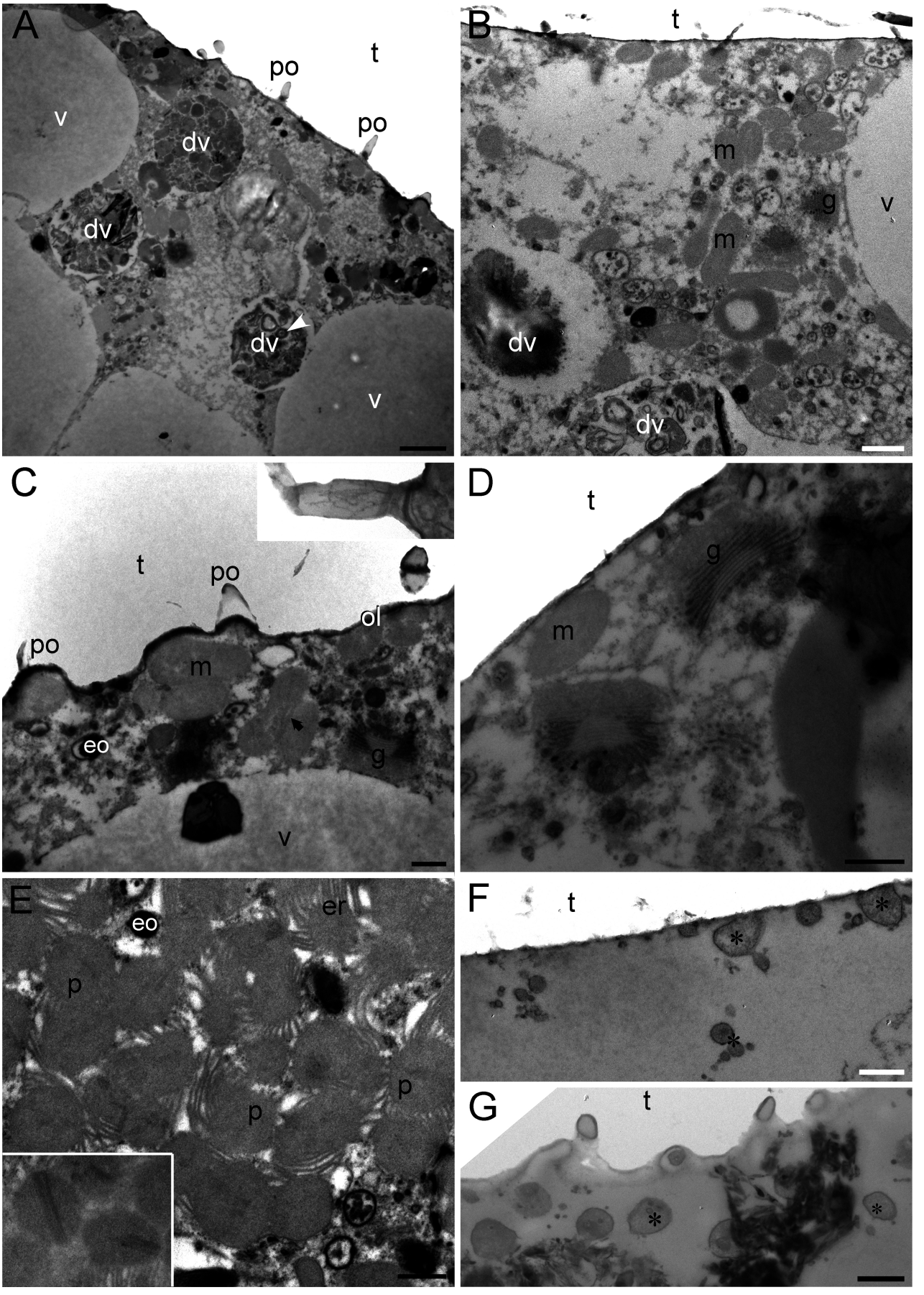
A
t
po
po
v
dv
dv
dv
v
B
t
m
g
v
m
dv
dv
C
t
po
ol
po
m
eo
g
v
D
t
g
m
E
eo
er
p
p
p
F
t
G
t

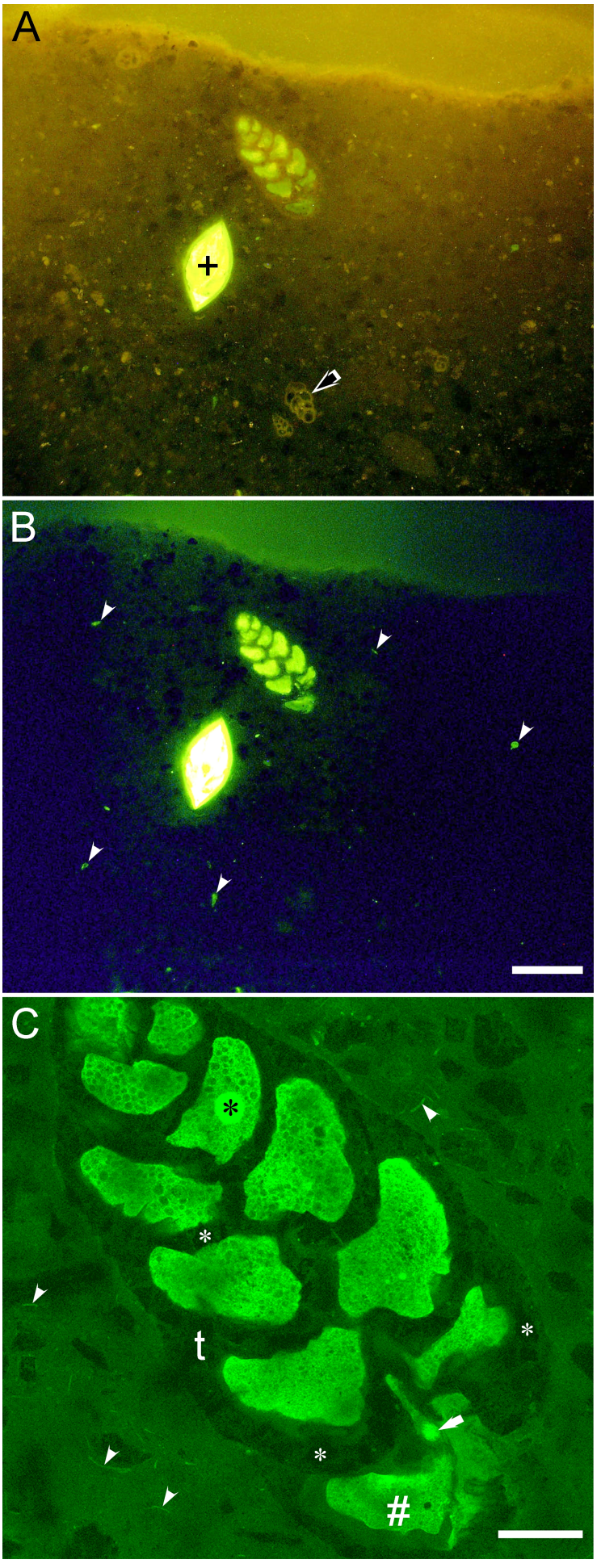
A
+
B
C
*
*
*
*
t
#

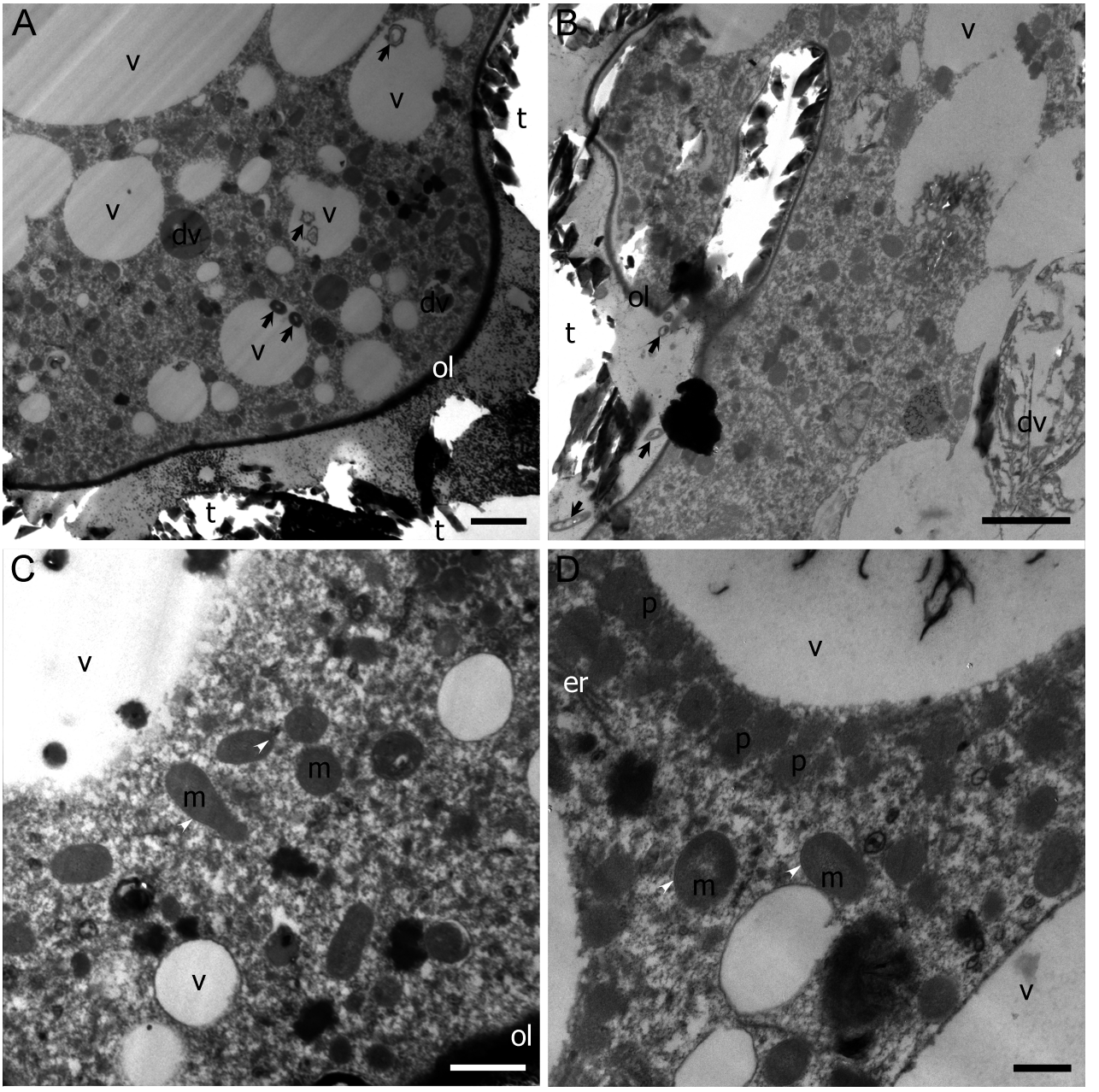
A
v
v
t
v
dv
v
dv
v
ol
t
t
B
v
ol
t
dv
C
v
m
m
v
ol
D
p
v
er
p
p
m
m
v

Figure 5

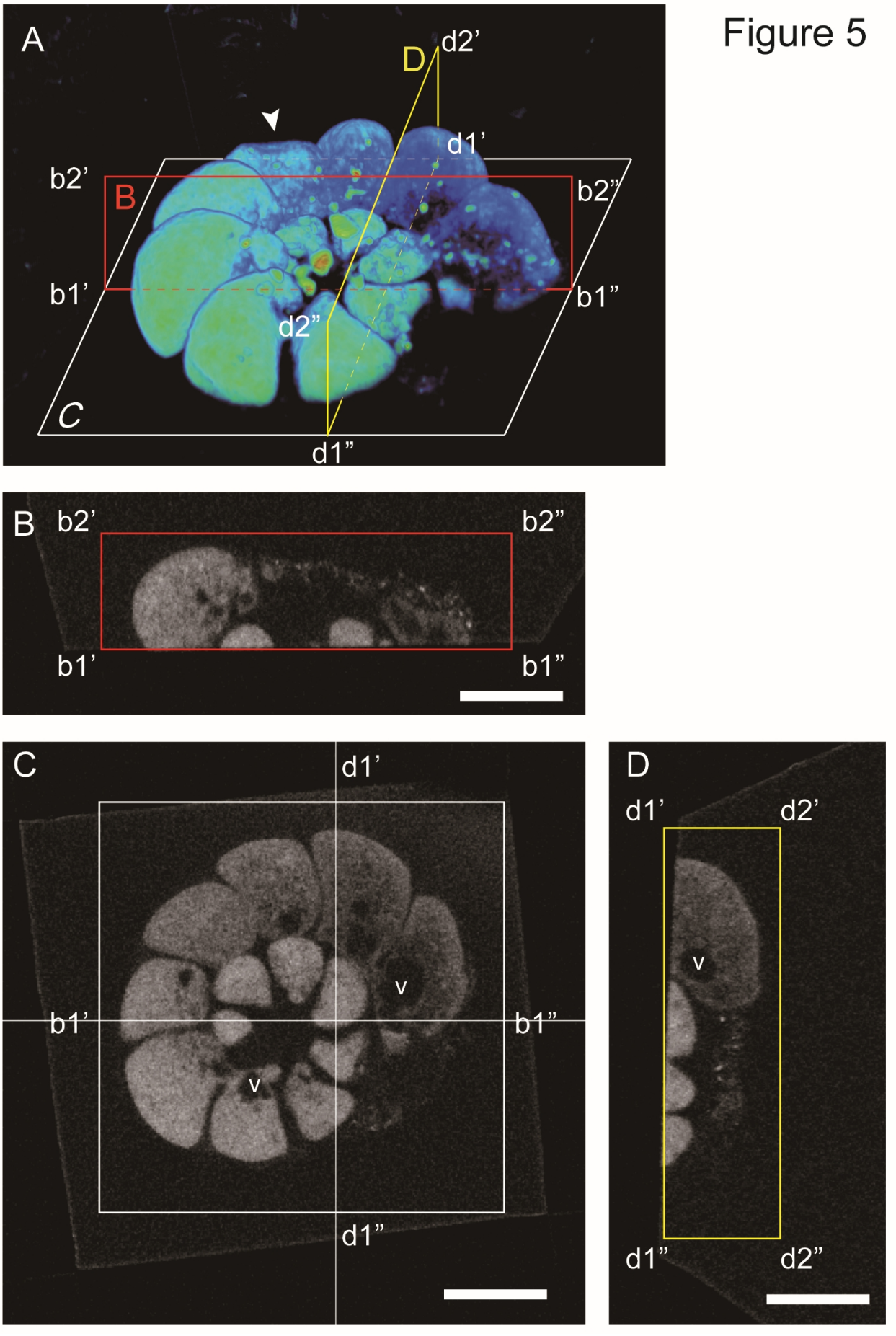
A
D
d2'
d1'
b2'
B
b2"
b1'
b1"
d2"
C
d1"
B
b2'
b2"
b1'
b1"
C
d1'
v
b1'
b1"
v
d1"
D
d1'
d2'
v
d1"
d2"

Figure 6

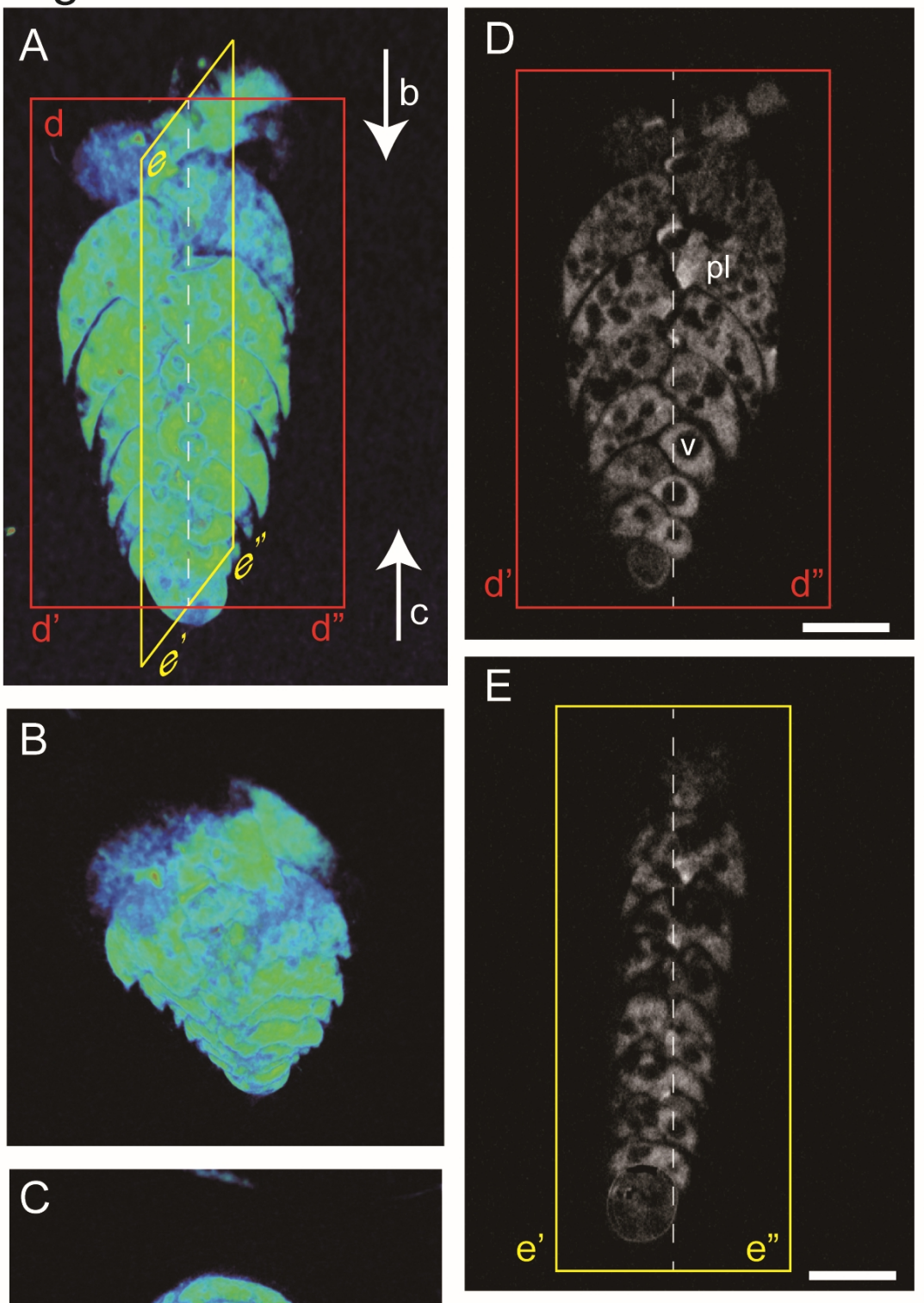

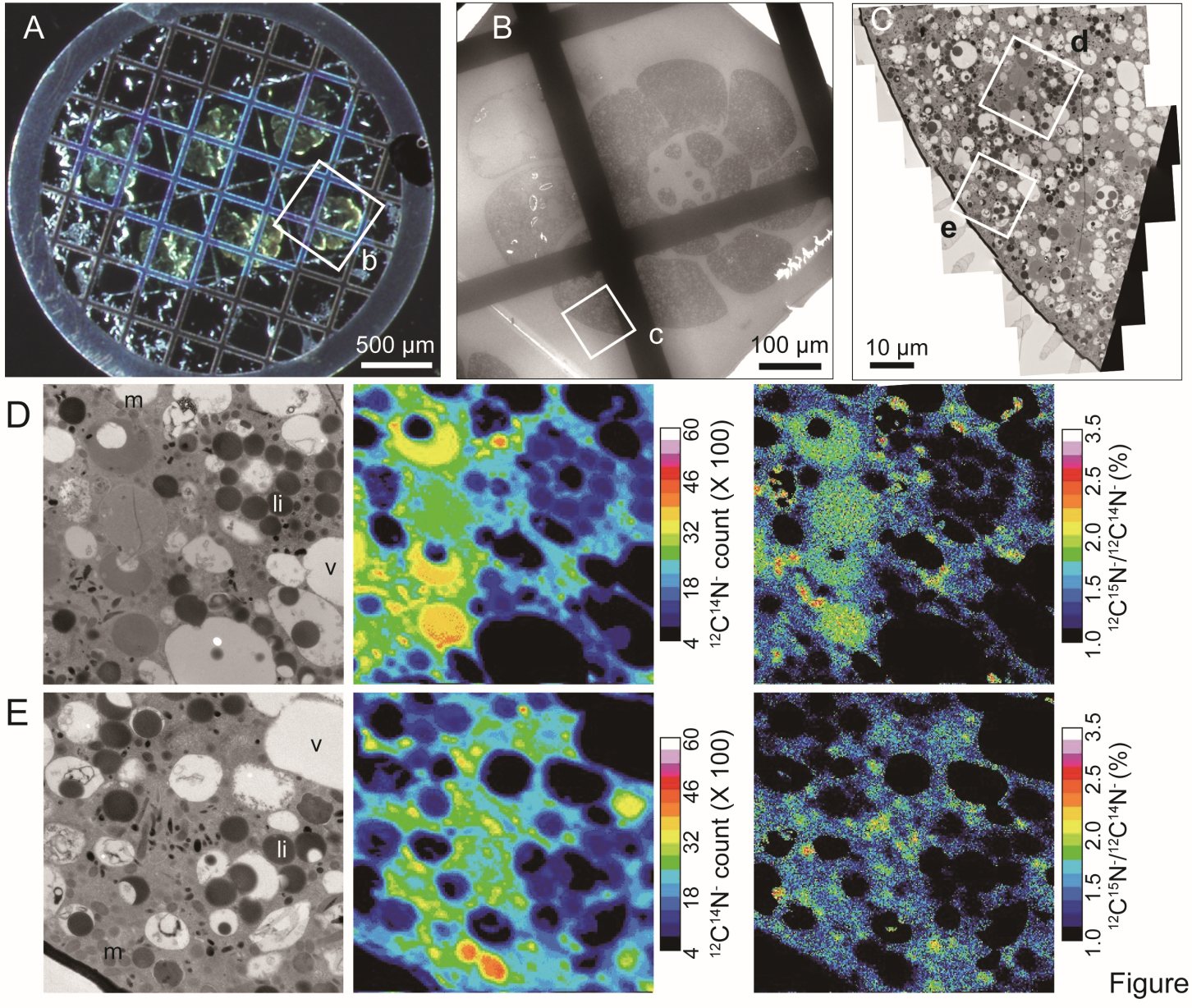
A
b
500 µm
B
c
100 µm
C
d
e
10 µm
D
m
li
v
4 18 32 46 60
$^{12}C^{14}N^-$ count (X 100)
1.0 1.5 2.0 2.5 3.5
$^{12}C^{15}N^-/^{12}C^{14}N^-$ (%)
E
v
li
m
4 18 32 46 60
$^{12}C^{14}N^-$ count (X 100)
1.0 1.5 2.0 2.5 3.5
$^{12}C^{15}N^-/^{12}C^{14}N^-$ (%)

Figure 7

Figure 8

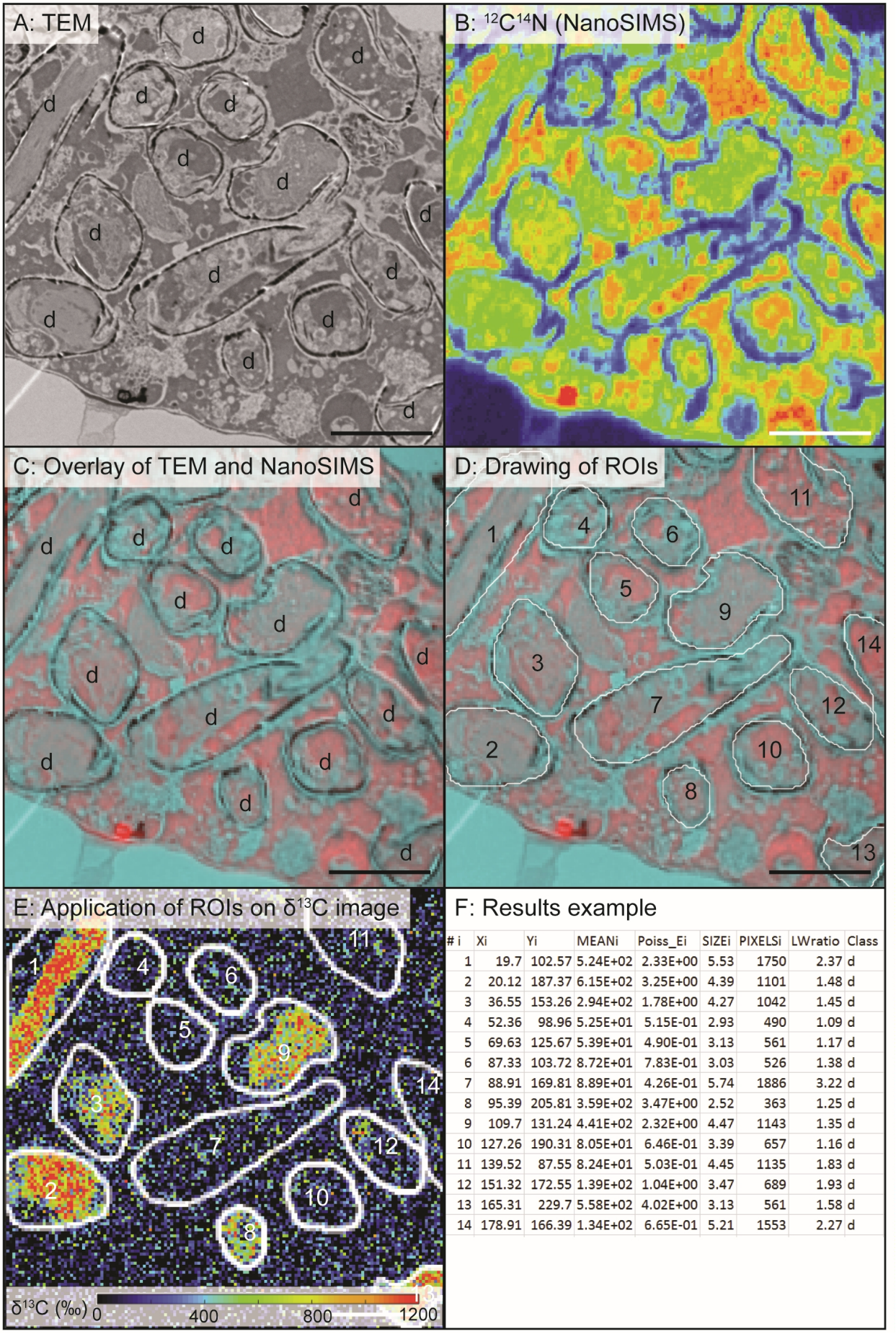

# i	Xi	Yi	MEANi	Poiss_Ei	SIZEi	PIXELSi	LWratio	Class
1	19.7	102.57	5.24E+02	2.33E+00	5.53	1750	2.37	d
2	20.12	187.37	6.15E+02	3.25E+00	4.39	1101	1.48	d
3	36.55	153.26	2.94E+02	1.78E+00	4.27	1042	1.45	d
4	52.36	98.96	5.25E+01	5.15E-01	2.93	490	1.09	d
5	69.63	125.67	5.39E+01	4.90E-01	3.13	561	1.17	d
6	87.33	103.72	8.72E+01	7.83E-01	3.03	526	1.38	d
7	88.91	169.81	8.89E+01	4.26E-01	5.74	1886	3.22	d
8	95.39	205.81	3.59E+02	3.47E+00	2.52	363	1.25	d
9	109.7	131.24	4.41E+02	2.32E+00	4.47	1143	1.35	d
10	127.26	190.31	8.05E+01	6.46E-01	3.39	657	1.16	d
11	139.52	87.55	8.24E+01	5.03E-01	4.45	1135	1.83	d
12	151.32	172.55	1.39E+02	1.04E+00	3.47	689	1.93	d
13	165.31	229.7	5.58E+02	4.02E+00	3.13	561	1.58	d
14	178.91	166.39	1.34E+02	6.65E-01	5.21	1553	2.27	d

Figure 9

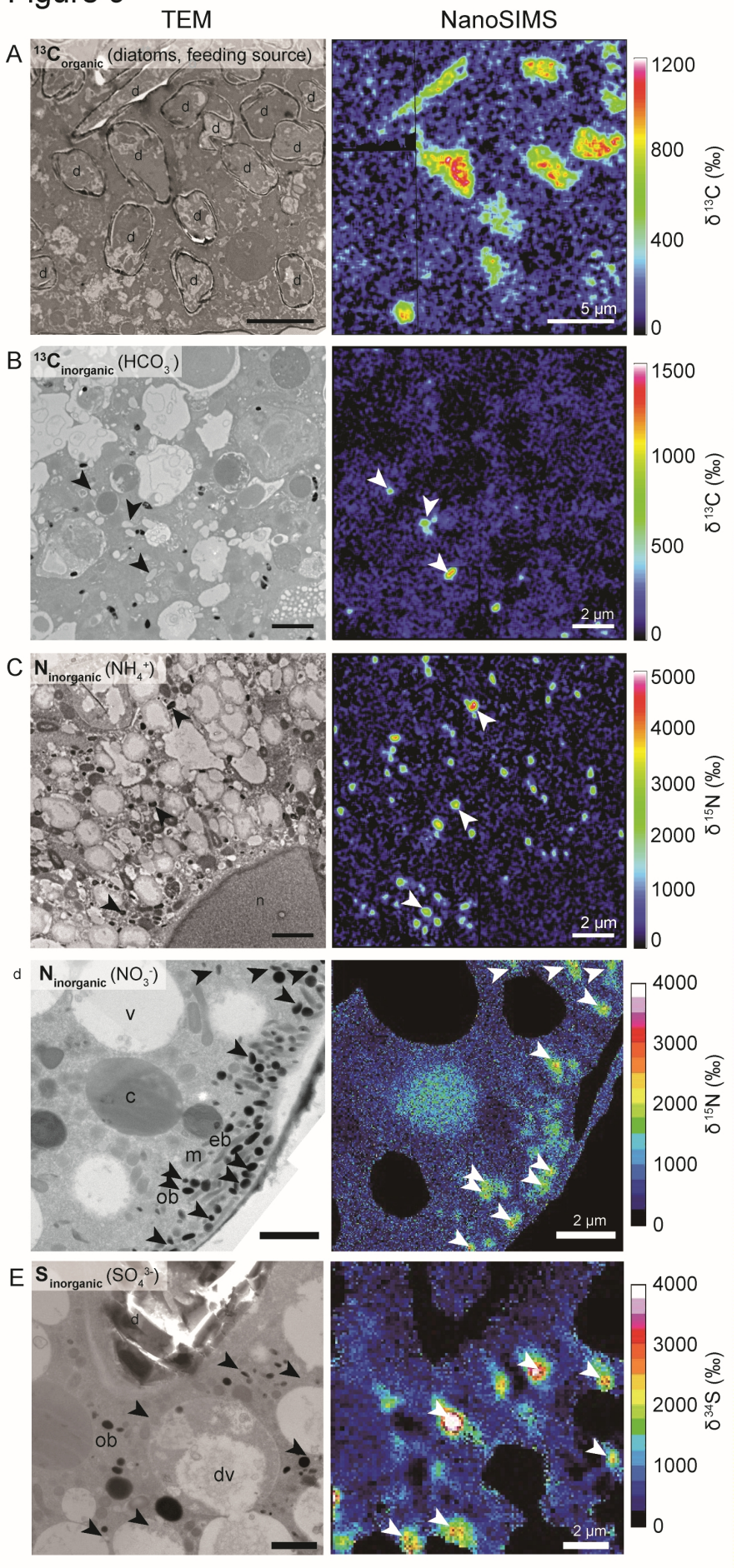
TEM
NanoSIMS
A
$^{13}C_{organic}$ (diatoms, feeding source)
d
5 µm
1200
800
400
0
$\delta^{13}C$ (‰)
B
$^{13}C_{inorganic}$ (HCO_3^-)
2 µm
1500
1000
500
0
$\delta^{13}C$ (‰)
C
$N_{inorganic}$ (NH_4^+)
n
2 µm
5000
4000
3000
2000
1000
0
$\delta^{15}N$ (‰)
d
$N_{inorganic}$ (NO_3^-)
v
c
eb
m
ob
2 µm
4000
3000
2000
1000
0
$\delta^{15}N$ (‰)
E
$S_{inorganic}$ (SO_4^{3-})
d
ob
dv
2 µm
4000
3000
2000
1000
0
$\delta^{34}S$ (‰)

Table 1. Incubation periods and stable isotope labels used for TEM-NanoSIMS analyses.

Species	Incubation period	Added isotope label
Ammonia sp. phytotype T6[1]	24 h	^{13}C-enriched diatom biofilm
Haynesina germanica [1]	16 h	$NaH^{13}CO_3$
Nonionellina labradorica [1]	7 h	$^{15}NH_4Cl$
Ammonia sp. phylotype T6[2]	14 d	$NaH^{13}CO_3$, $Na^{15}NO_3$, $Na_2{}^{34}SO_4$

[1] LeKieffre et al. (2017 and unpublished data)

[2] Nomaki et al. (2016)

Table 2. NanoSIMS measurement settings of Nomaki et al. (2016) and LeKieffre et al. (2017 and unpublished data).

	$^{13}C/^{12}C$, $^{15}N/^{14}N$ analyses[1]	$^{15}N/^{14}N$ analyses[2]	$^{34}S/^{32}S$ analysis[2]
Measurement area	15×15 or 30×30 µm (256×256 pixels)	Typically 8×8 to 15×15 µm (256×256 pixels)	Typically 8×8 to 16×16 µm (128×128 or 256×256 pixels)
Primary beam	about 2 pA Cs^+ beam	about 1 pA Cs^+ beam	about 5 pA Cs^+ beam
Primary beam focus size	120-150 nm	< 600 nm	< 1000 nm
Primary beam dwell-time	5 milliseconds/pixel	< 1 millisecond/pixel	< 1 millisecond/pixel
Mass resolution	8000-10000 at 10% peak height	> 8000 at 10% peak height	> 8000 at 10% peak height
Numbers of sequential image at 1 site	6 to 10	Typically 50	Typically 20

[1] LeKieffre et al. (2017 and unpublished data)

[2] Nomaki et al. (2016)